Mineralium Deposita
https://doi.org/10.1007/s00126-019-00899-z

ARTICLE

Evolution of the subseafloor hydrothermal system associated with the Ming VMS deposit, Newfoundland Appalachians, and its controls on base and precious metal distribution

Jean-Luc Pilote[1,2] · Stephen J. Piercey[1] · Patrick Mercier-Langevin[2]

Received: 8 January 2018 / Accepted: 13 May 2019

Abstract

The ~ 487 Ma Ming volcanogenic massive sulfide (VMS) deposit consists of four subparallel, elongated, semi-massive to massive sulfides lenses (the 1807, 1806, Ming North, and Ming South zones) hosted in rhyodacite of the Rambler Rhyolite formation, Newfoundland Appalachians. A discordant Cu-rich Lower Footwall zone underlies the semi-massive to massive sulfide lenses. Alteration associated with mineralization can be divided into nine facies that formed in three paragenetic stages: (1) weak quartz–calcite ± spessartine, quartz–sericite, and quartz–sericite–chlorite alteration (stage 1); (2) quartz–chlorite, quartz–chlorite–sulfide, and quartz–chlorite–sericite assemblages (stage 2); and (3) quartz–sericite–sulfide and localized Mn-rich carbonate assemblages (stage 3). A thin syngenetic silica-rich layer immediately overlies part of the VMS deposit and likely formed during the early stages. The volcanic architecture and synvolcanic faults controlled the lateral distribution of extrusive rocks and hydrothermal alteration. Precipitation of the high temperature, discordant to semi-conformable Cu-rich chloritic assemblages (stockwork), was laterally restricted to one of these synvolcanic faults and the transition from coherent- to volcaniclastic-dominated lithofacies. Lower temperature, sericitic assemblages (stages 1 and 3) are controlled by the distribution of volcaniclastic rocks and generally form the immediate footwall to the semi-massive to massive sulfide lenses. Lithogeochemical mass balance calculations illustrate the alteration minerals and mineralization: chlorite-rich assemblages—gains in SiO_2, Fe_2O_3t, MgO, Cr, Ni, and Cu and losses in Na_2O, MnO, and CaO and sericite-rich assemblages—gains in K_2O, Zn, and Ag and losses in MnO, MgO, CaO, Na_2O, and Y. Calcium- and magnesium-rich alteration assemblages are restricted to the northwest fringe of the deposit, distal to the main chloritic and sericitic alteration, and have elemental gains in P_2O_5, Y, and losses in K_2O. The late stage 3 quartz–sericite–sulfide assemblage overprints most assemblages, hosts sphalerite–galena–sulfosalt–Ag–Au-rich veins, and is spatially associated with coherent volcanic rocks. The less permeable nature of these rocks is interpreted to have acted as a physical barrier for ascending metal-rich hydrothermal fluids. Results from the detailed reconstruction of the hydrothermal architecture and paragenetic evolution of the Ming deposit suggest that precious metals were introduced during the waning stage of the hydrothermal system, associated with decreases in temperature and pH of the hydrothermal fluids.

Keywords Appalachians · Baie Verte · VMS alteration · Mineralogy · Mineral chemistry · Hyperspectral reflectance spectrometry · Precious metal enrichment

Editorial handling: K. Kelley

Electronic supplementary material The online version of this article (https://doi.org/10.1007/s00126-019-00899-z) contains supplementary material, which is available to authorized users.

✉ Jean-Luc Pilote
jean-luc.pilote@canada.ca

[1] Department of Earth Sciences, Memorial University of Newfoundland, 300 Prince Philip Drive, St. John's, Newfoundland and Labrador A1B 3X5, Canada

[2] Geological Survey of Canada, 490 rue de la Couronne, Québec, Québec G1K 9A9, Canada

Introduction

The ~ 487 Ma Ming deposit is a polymetallic Cu–Zn–Ag–Au volcanogenic massive sulfide (VMS) deposit within the Pacquet ophiolite complex located in the northern Newfoundland Appalachians (Fig. 1; van Staal and Barr 2012). To date, a total of 0.8 Mt grading 2.9% Cu, 9.63 g/t Ag, and 1.38 g/t Au were processed, with combined measured and indicated resources of almost 28 Mt averaging 1.48% Cu, 0.06% Zn, 1.99 g/t Ag, and 0.26 g/t Au (as of November 2016; Rambler Metals and Mining Ltd., pers. comm. 2017). Much like other well-preserved (in respect to the overall

Published online: 08 July 2019

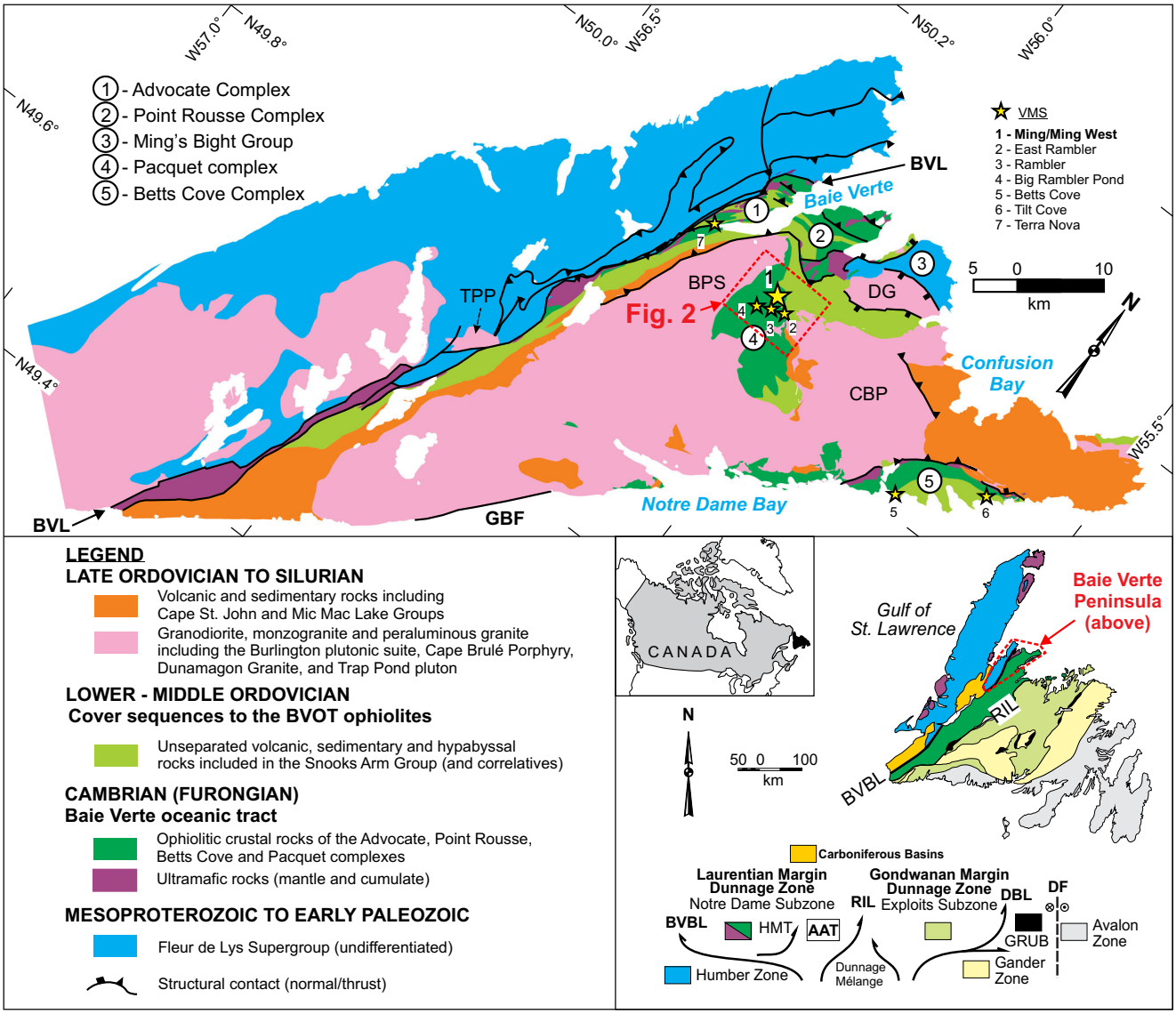

Fig. 1 Simplified geology of the Baie Verte Peninsula with major tectonostratigraphic zones that form the Appalachian orogenic belt in Newfoundland (modified from Castonguay et al. 2014). Location of major VMS deposits as yellow stars. AAT Annieopsquotch Accretionary Tract, BPS Burlington plutonic suite, BVBL Baie Verte-Brompton Line, BVL Baie Verte Line, CB Cape Brulé Porphyry, DBL Dog Bay Line, DF Dover Fault, DG Dunamagon Granite, GBF Green Bay Fault, GRUB Gander River Ultramafic Belt, TPP Trap Pond pluton, RIL Red Indian Line, HMT Hungry Mountain Thrust

deposit architecture), but metamorphosed VMS deposits (e.g., Flin Flon, LaRonde Penna; DeWolfe 2009; Dubé et al. 2007; Mercier-Langevin et al. 2007), the Ming deposit is a good example of a mound-style VMS deposit associated with a well-developed, extensive, and zoned footwall alteration (Pilote et al. 2017). Despite the structural complexity near the massive sulfide horizon and the regional upper greenschist metamorphic overprint (Castonguay et al. 2014), the overall relationship between the mineralization and its altered host rocks is well preserved and relatively intact (Tuach and Kennedy 1978; Pilote et al. 2017).

Despite several studies on the Ming deposit (Brueckner et al. 2011, 2014, 2015, 2016; Pilote et al. 2016, 2017), and historical research (Gale 1971; Tuach and Kennedy 1978; Bailey 2002), very little is known about the alteration associated with this Appalachian VMS deposit, largely because of the lack of detailed geological and structural information that inhibited the characterization and contextualization of the hydrothermal alteration. In the Ming deposit, accessibility to underground workings and drill core from closely spaced surface and underground drill holes offers an ideal opportunity to study, in detail, the hydrothermal alteration associated with the Ming deposit. Correspondingly, the aim of this paper is to document the mineralogy, mineral assemblages, paragenesis, and distribution of alteration in the Ming VMS deposit; assess the genetic relationships between mineralization and alteration

assemblages; and define the physical and chemical processes responsible for the alteration and the nature of fluid–rock interaction. The approach combines field observations, geochemical, mineralogical, mineral chemical, and infrared spectroscopic data to understand the nature and distribution of alteration, the chemical fluxes associated with alteration, and better understanding of the volcanic and structural control on hydrothermal fluids and their evolution in space and time. Because of the relatively well-preserved nature of the Ming VMS deposit and its alteration envelope, this detailed study provides insights into fluid–rock interaction processes associated with precious metal deportment in massive sulfide deposits and the generation of precious metal-bearing deposits in modern and ancient VMS deposits worldwide.

Geologic setting

Regional geology

The Ming deposit, Baie Verte Peninsula, Newfoundland, is hosted within the structurally segmented Upper Cambrian to Lower Ordovician ophiolitic rocks of the supra-subduction Baie Verte oceanic tract (Waldron and van Staal 2001; van Staal and Barr 2012; van Staal et al. 2013). The Baie Verte oceanic tract is fault bounded to the west by the Baie Verte Line, where it is juxtaposed against the Neoproterozoic to Upper Cambrian metasedimentary rocks of the ancient Laurentian margin (Fleur de Lys Supergroup) (Fig. 1; van Staal and Barr 2012). In the east, it is in fault contact with the Middle to Upper Cambrian (510–501 Ma) Lushs Bight oceanic tract along the Green Bay Fault (van Staal and Barr 2012). The ophiolitic rock of the Baie Verte Peninsula (Betts Cove, Pacquet, Pointe Rousse, and Advocate complexes) is interpreted to represent remnants of a single VMS-hosting ~ 490 Ma ophiolitic sheet (Hibbard 1983; Dunning and Krogh 1985; Cawood et al. 1996; Bédard and Escayola 2010; Skulski et al. 2010, 2015). The ophiolitic rocks represent variably preserved forearc assemblages that contain variably serpentinized mantle rocks, overlain by ultramafic cumulate sections, isotropic gabbros to sheeted dikes, and pillowed boninites of the Betts Head Formation (Bédard et al. 1996). The Betts Head Formation is overlain by mafic island arc tholeiites and felsic volcanic rocks of the Mount Misery and Rambler Rhyolite formations, respectively (Fig. 2). Collectively, the volcanic rocks of the Baie Verte oceanic tract reach a maximum thickness of 5 km in the Pacquet complex, including the (informal) Rambler Rhyolite formation, which is host to the Ming deposit. The ophiolite complexes are unconformably overlain by and structurally imbricated with the Lower to Middle Ordovician volcano–sedimentary successions of the Snooks Arm Group (Skulski et al. 2010, 2015).

Local geology

The Rambler Rhyolite formation is a ~ 3 × 5-km dome-shaped complex located in a northeast-plunging anticlinal fold structure and is underlain by the mafic-dominated Mount Misery Formation (Fig. 2; Castonguay et al. 2014; Pilote et al. 2017). The upper 1000 m of the Rambler Rhyolite formation (Pilote et al. 2017) consists of the following: (1) coherent quartz–phyric to aphanitic felsic volcanic rocks (unit 1.1), sharply transitioning upwards to (2) bedded to massive quartz-bearing felsic volcaniclastic rocks (unit 1.2), overlain by (3) a thin blue quartz–phyric to quartz–megacrystic coherent felsic flows that laterally transition to bedded quartz-bearing felsic tuffs (unit 1.3) (Fig. 3). The distribution of units 1.2 and 1.3 reflects deposition proximal to rift-related synvolcanic faults (Pilote et al. 2017). The massive- to semi-massive sulfides at Ming are located at the very top of the felsic flow complex and have a 30–35° plunge. There are five zones in the deposit: the 1807, 1806, Ming North, Ming South, and the Lower Footwall zones (Fig. 2). These have significant variations in Cu, Zn, Ag, and Au grades with the 1806 zone having elevated Ag and Au (averaging 15.07 g/t and 2.97 g/t, respectively; Brueckner et al. 2014, 2016; Pilote et al. 2017). The Lower Footwall zone represents a Cu-rich stockwork that is interpreted to be the feeder zone of the deposit.

Metamorphism and deformation

The Pacquet complex has upper greenschist facies metamorphic assemblages, except near the Ordovician–Silurian intrusive bodies, where it locally reaches amphibolite facies (Tuach and Kennedy 1978; Castonguay et al. 2009, 2014). Four major deformation events (D_1 to D_4) are recognized at the Ming deposit (Pilote et al. 2017). The earliest fabric (D_1) consists of a poorly preserved foliation that has been strongly overprinted by D_2 deformation (Castonguay et al. 2009, 2014; Pilote et al. 2017). D_2 consists of a northeast-striking, moderately dipping schistosity (S_2) and a northeast plunging stretching lineation (L_2) that rakes along S_2. Sulfides are locally transposed and/or remobilized into D_2 structures, resulting in piercement structures and oreshoots, normal to S_2 and along stratigraphic or lithologic contacts. D_2 structures are accentuated by overprinting boudinage-related (D_3) deformation and a discrete D_4 cleavage; however, despite deformation, sulfide remobilization is spatially restricted to a few centimeters, up to 20 m from the ore bodies (Pilote et al. 2017). The synvolcanic hydrothermal alteration assemblages at Ming were metamorphosed to greenschist facies, and the different assemblages described below are metamorphic equivalents of the alteration assemblages that developed during ore formation; however, it appears that there has been only minor modification of the original VMS-related assemblages after regional deformation and metamorphism.

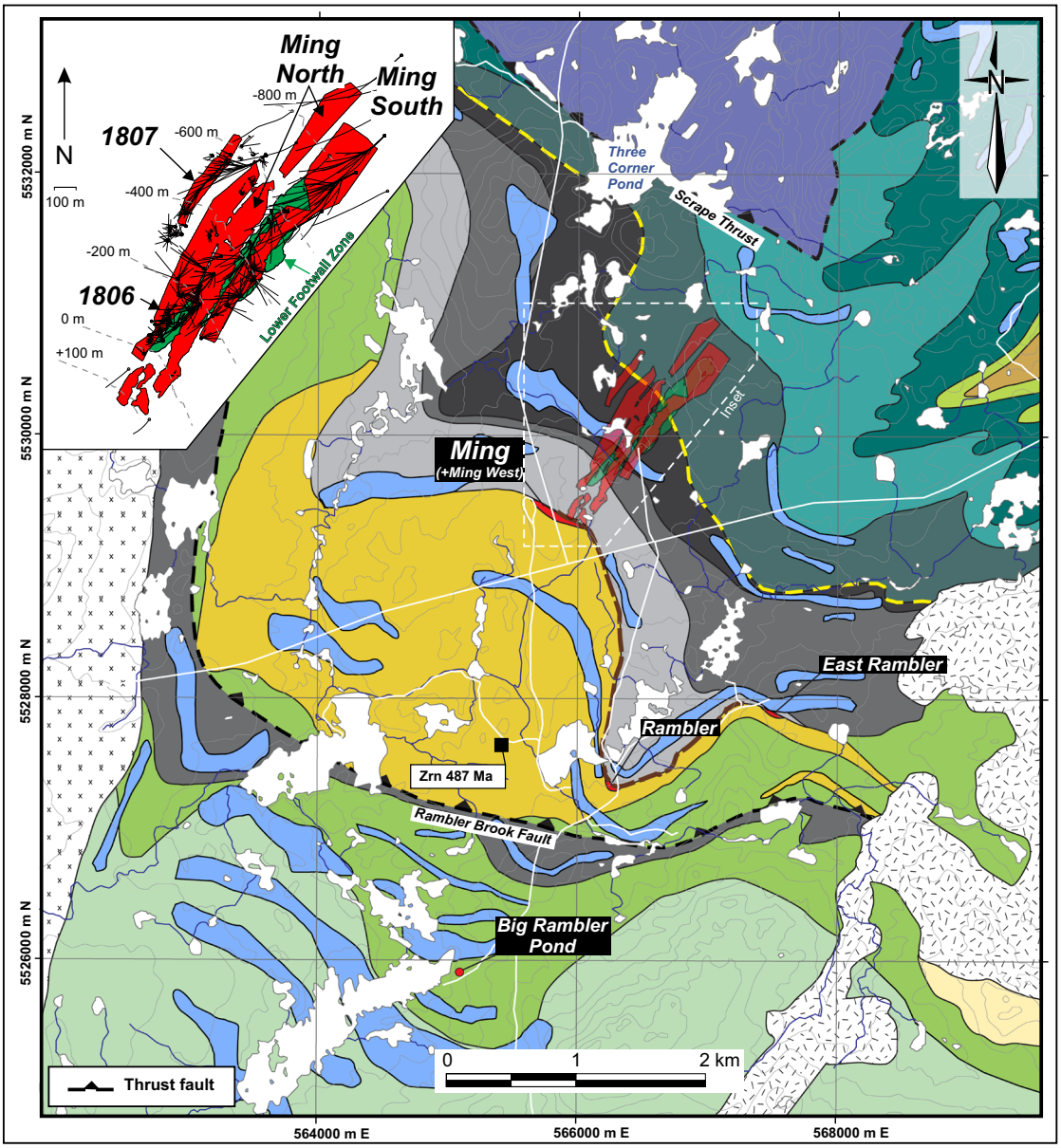

Silurian Cape St. John Group (unseparated)

Clastic, pink-red sedimentary rocks, mafic and/or felsic volcanic rocks.

Burlington Granodiorite (434 - 430 Ma)

Cape Brulé Porphyry (430 Ma)
Porphyritic granodiorite, quartz-feldspar porphyry.

Early-Middle Ordovician Snooks Arm Group (479-467 Ma)

Tholeiitic gabbro sills/dikes, include plagioclase-phyric to fine-grained gabbro. Minor medium-grained equigranular diorite.

Basalm Bud Cove Formation

Volcanogenic turbidite, siltstone, felsic tuffs, basalts.

Calc-alkaline felsic tuff, lapilli tuff.

Venam's Bight Formation
Tholeiitic pillowed basalt, porphyritic and vesicular basalt, siliceous mudstone.

Bobby Cove Formation
Chert, iron formation, volcanogenic sedimentary rocks, minor felsic tuffs.

Mafic tuff, lapilli tuff, epiclastic rocks, interbedded basalt flows.

Clinopyroxene-phyric crystal tuff, lapilli tuff, and tuff breccia (Prairie Hat member).

Calk-alkaline plagioclase-phyric pillow basalt and andesite.

Scrape Point Formation
Mafic volcaniclastic rocks, tuff, lapilli tuff, epiclastic sandstone, shale, interbedded pillow basalt.

Pillowed, massive, amygdaloidal, plgioclase-phyric basalt flows. Tholeiitic affinities.

Magnetite-rich iron formation, chert beds, volcanogenic siltstone (Nugget Pond horizon).

Cambro-Ordovician Pacquet complex

Rambler Rhyolite formation (487 Ma)
Calc-alkalic quartz-phyric rhyolite to rhyodacite flows interbedded with intermediate to felsic tuff, lapilli tuffs, and tuff breccia.

Mt. Misery Formation
Plagioclase- and pyroxene-phyric pillow basalt with tholeiitic affinities, interbedded with boninite.

Betts Head Formation
Spherulitic, amygdaloidal, porphyritic boninitic pillow lavas with aphanitic dark-green groundmass.

Point Rousse ophiolite (490 Ma)

Undifferentiated serpentinized ultramafic rocks with tholeiitic and boninitic affinities.

◀ **Fig. 2** Geological map of the study area, Baie Verte Peninsula, with Ming VMS orebodies projected to surface (also in the inset) and shown in light red and light green (Lower Footwall zone = stockwork). Datum is UTM 21N NAD 83. Map compiled and modified from Tuach and Kennedy (1978), Hibbard (1983), Castonguay et al. (2009), Pilgrim (2009), and Skulski et al. (2010). The U–Pb zircon (Zrn) age is from Skulski et al. (2015). The Ming South, Ming North, 1806, and 1807 mineralized zones are identified in the inset

Hydrothermal alteration

Alteration facies, mineral assemblages, and their distribution

Field and drill core observations, coupled with petrography and analytical methods, were used to map the alteration mineral assemblage distributions, inter-relationships, and paragenesis (Table 1; Fig. 4; Electronic supplementary material (ESM) 1 Fig. 1). Two principal extensive alteration facies are recognized at the Ming deposit: a chlorite-rich facies that is formed 50 to 300 m below the massive sulfide horizon and a sericite-rich facies (Rieder et al. 1999), formed within ~ 100 m of the massive sulfides and within and below the chlorite-rich facies (Fig. 4); both facies are subparallel to the northeast-plunging ore zones. Other less extensive alteration assemblages include weakly altered and Mn-rich garnet-bearing facies that are developed in the immediate footwall of the 1807. A stratiform silica-rich horizon forms a < 3-m layer in the immediate hanging wall to mineralization in the 1806 and 1807 zones (Fig. 4).

Chlorite-rich alteration facies

The chlorite-rich alteration facies is divided into the following: (1) quartz–chlorite, (2) quartz–chlorite–sulfide, and (3) quartz–chlorite–sericite subfacies (Fig. 4; ESM 1 Fig. 1). The first two assemblages are found in units 1.1 and 1.2 with the rocks having pervasive quartz and chlorite alteration, which are overprinted by fine- to coarse-grained metamorphic minerals (likely M_2) consisting of actinolite, epidote, and biotite (Fig. 5a). The chlorite alteration facies forms a > 2000-m × ~ 400-m discordant to semi-conformable alteration zone; discordant zones contain centimeter-scale sulfide-rich stringers. The quartz–chlorite–sulfide assemblage is restricted to below the Ming South zone, the up-dip section of the 1806 zone, and the Lower Footwall zone, where it is associated with the footwall feeder zone to the deposit (Figs. 4 and 5b). The quartz–chlorite–sericite assemblage represents the less intense alteration assemblage of the chlorite-rich facies and occurs within units 1.1 and 1.2 in the Ming South and 1807 zones and is commonly found marginal to or within the quartz–chlorite and quartz–chlorite–sulfide assemblages; this assemblage also occurs in the 1806 zone (Fig. 4).

Sericite-rich alteration facies

The sericite-rich facies is subdivided into three main mineral assemblages: (1) quartz–sericite–chlorite, (2) quartz–sericite, and (3) quartz–sericite–sulfide (Table 1). Most of the sericite-rich facies is limited to within ~ 100 m of mineralization, except for the quartz–sericite–chlorite assemblage; however, all are limited to below the Ming South and 1806 zones (Fig. 4). The quartz–sericite–chlorite assemblage is light to intermediate gray with very fine-grained quartz and sericite (Fig. 5a) and occurs as < 25-m-thick intersections within coherent and volcaniclastic rocks of units 1.1 and 1.2 (Fig. 4); at depth, this assemblage is cut by quartz and chlorite associated with the high-temperature, proximal chlorite alteration. Both the quartz–sericite and quartz–sericite–sulfide assemblages are light to intermediate greenish gray and with trace chlorite (Fig. 5d, e) and variable millimeter- to centimeter-scale clots and fine-grained green mica (Figs. 4 and 6a) and predominantly occur within the coherent and tuffaceous facies of units 1.2 and 1.3 (Fig. 4). Within the sericitic facies, fine epidote grains are found exclusively in the quartz–sericite assemblage (ESM 1 Fig. 1). Sulfide stringers are restricted to the sericite-rich alteration and consist of galena and pyrrhotite (Table 1; Fig. 5e; ESM 1 Fig. 1). The temporal relationships between the quartz–sericite and quartz–sericite–sulfide assemblages are cryptic; however, there is a sharp contact between the chloritic facies and the quartz–sericite–sulfide facies on level 1450 below the 1806 zone (Fig. 6b, c; ESM 1 Fig. 2), suggesting that the quartz–sericite–sulfide assemblage was one of the paragenetically latest assemblages in the deposit.

Weak alteration facies

A weak alteration is developed < 10 m in the footwall of the 1807 zone and to a depth of ~ 30 m into the 1806 and Ming South zones (Fig. 4). The assemblage consists of sericite, chlorite, and other trace minerals (ESM 1 Fig. 1), typically developed in the groundmass of the coherent to volcaniclastic rocks (Fig. 5f). The weakly altered rocks are purplish gray with plagioclase altered to sericite, and this alteration transitions laterally and stratigraphically to a slightly more intense alteration assemblage composed of sericite, porphyroblastic Mn-garnet (spessartine), and calcite (Pilote et al. 2014) (Fig. 5g, h). A paragenetically late network of veins composed of calcite, quartz, and spessartine cross-cut other alteration assemblages proximal (< 10 m) to the massive sulfides of the 1807 zone (Fig. 5h).

Silica-rich layer

The stratiform silica-rich layer that immediately overlies the 1806 zone consists of a gray colored, massive, and featureless quartz–calcite-rich assemblage (Fig. 4). It is in sharp contact

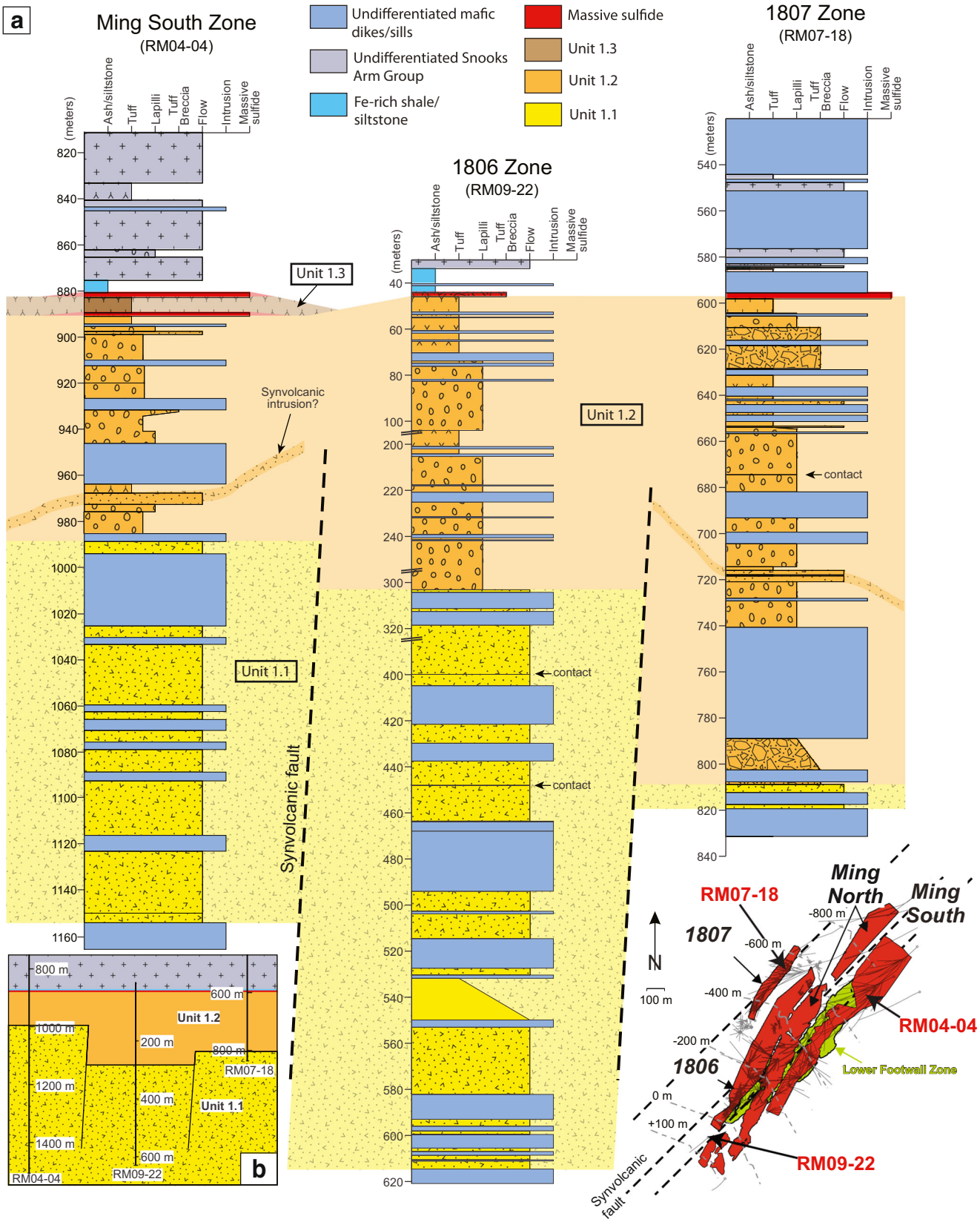

with the overlying cover sequence and neither does cross-cut nor does it replace surrounding units (no evidence of relic clasts). Recrystallized, fine-grained, cubic disseminated pyrite grains are found throughout this layer. As well, chalcopyrite,

◀ **Fig. 3** **a** Composite stratigraphic columns of the Ming South (DDH RM04-04), 1806 (RM09-22), and 1807 (RM07-18) zones (after Pilote et al. 2017). This reconstruction illustrates the volcaniclastic lithofacies (fragment, "Y," and circle fill patterns) associated with all zones. Note the downhole breaks of lengths in drill hole RM09-22. The synvolcanic faults are interpreted based on the sharp lateral change in lithofacies and on the distribution of the chlorite-rich alteration assemblages spatially and genetically associated with the Lower Footwall zone. **b** Simplified cross section of **a** with no downhole breaks, showing complete stratigraphic thicknesses. The drill holes are correlated across the sulfide lenses

sphalerite, and electrum (Au–Ag alloy) veinlets are developed as D_2-related piercement structures, at high angle to the main S_2 fabric (Pilote et al. 2017).

Hyperspectral data

Hyperspectral analyses were undertaken on altered samples to evaluate hydroxyl-bearing mineral such as micas and chlorite

Table 1 Summary of the mineralogy and elemental changes within the various hydrothermal alteration assemblages at the Ming deposit

Alteration assemblage[1]	Zone	Major minerals (vol%)[2]	Minor and trace minerals (vol%)[2]	Main elemental changes[3]
1. Weak alteration	1807 zone (± 1806 and Ming South zones)	Quartz (≤ 76), epidote (≤ 30), plagioclase (≤ 20), sericite (≤ 25), biotite (≤ 20), actinolite (≤ 15), chlorite (≤ 15)	Calcite, pyrite, chalcopyrite, pyrrhotite, magnetite, ilmenite	Losses: MnO, Na_2O, Y Gains: SiO_2, Fe_2O_{3t}, MgO, CaO, P_2O_5
2. Sericite–calcite ± spessartine	1807 zone (± 1806 and Ming South zones)	Quartz (≤ 55), sericite (≤ 44), calcite (≤ 25), biotite (≤ 16), epidote (≤ 15)	Spessartine, plagioclase, chlorite, apatite, magnetite, pyrite, chalcopyrite, sphalerite, galena, rutile	Losses: Fe_2O_{3t}, MgO, Cr, Ni Gains: MnO, P_2O_5, Y, Cu
3. Quartz–sericite	1806 and Ming South zones (± 1807 zone)	Quartz (≤ 56), sericite (≤ 47)	Chlorite, biotite, epidote, pyrite, chalcopyrite, sphalerite, arsenopyrite, galena, sulfosalts, rutile, electrum?	Losses: SiO_2, MnO, MgO, CaO, Na_2O, P_2O_5 Gains: K_2O, Cr, Ni, Cu, Zn, Ag
4. Mn-rich carbonate	1807 zone	Quartz (35), Mn-rich calcite (21), spessartine (20)	Apatite, biotite, plagioclase	Losses: Na_2O, K_2O, Cr, Gains: MnO, CaO, P_2O_5, Y, Cu
5. Quartz–sericite –chlorite	1806 and Ming South zones	Quartz (≤ 55), sericite (≤ 45), chlorite (≤ 29)	Pyrite, biotite, chalcopyrite, pyrrhotite, sphalerite, epidote, magnetite, ilmenite, galena	Losses: MnO, CaO, Y, Cr, Ni Gains: SiO_2, Fe_2O_{3t}, MgO, K_2O, Cu, Ag
6. Quartz–chlorite	1807, 1806 and Ming South	Quartz (≤ 60), chlorite (≤ 47), biotite (≤ 30), actinolite (≤ 30)	Epidote, pyrite, chalcopyrite, pyrrhotite, sphalerite, plagioclase, magnetite, ilmenite, rutile, calcite, sericite	Losses: MnO, CaO, Na_2O, K_2O, Y Gains: SiO_2, Fe_2O_{3t}, MgO, Cr, Ni, Cu
7. Quartz–chlorite –sulfide	1806 and Ming South zones	Quartz (≤ 65), chlorite (≤ 79), pyrite (≤ 20), chalcopyrite (≤ 20), actinolite (≤ 15)	Pyrrhotite (≤ 10), biotite, epidote, sphalerite, magnetite, ilmenite, sericite	Losses: MnO, CaO, Na_2O, K_2O, Y Gains: SiO_2, Fe_2O_{3t}, MgO, Cr, Ni, Cu, Ag
8. Quartz–chlorite–sericite (± sulfides)	1806 and Ming South zones	Quartz (≤ 55), chlorite (≤ 37), sericite (≤ 32)	Pyrite (≤ 6), chalcopyrite (≤ 6), pyrrhotite (≤ 4), epidote, biotite, magnetite, ilmenite, rutile, sphalerite, galena	Losses: MnO, CaO, Na_2O, Y Gains: SiO_2, Fe_2O_{3t}, MgO, Cr, Ni, Cu, Ag
9. Quartz–sericite –sulfide	1806 and Ming South zones	Quartz (≤ 63), sericite (≤ 46), pyrite (≤ 15)	Chalcopyrite, sphalerite, arsenopyrite, galena, sulfosalts, tellurides, Au–Ag alloys (e.g., electrum), chlorite, biotite, calcite, rutile	Losses: MnO, MgO, CaO, Na_2O, Y Gains: SiO_2, Fe_2O_{3t}, K_2O, Cu, Zn, Ag
10. Silica-rich layer/fragments	1806 zone (± 1807 zone)	Quartz (≤ 98), calcite (≤ 13)	Pyrite (≤ 4), chalcopyrite, sphalerite, biotite, epidote, electrum	Losses: MgO, Na_2O, K_2O Gains: SiO_2, Fe_2O_{3t}, MnO, CaO, P_2O_5, Y, Cr, Ni, Cu, Zn, Ag

[1] Combining units 1.1 to 1.3

[2] In brackets are the maximum relative amounts. Averages are presented in ESM1 Fig.1

[3] Based on mass balance calculations presented in Fig. 12

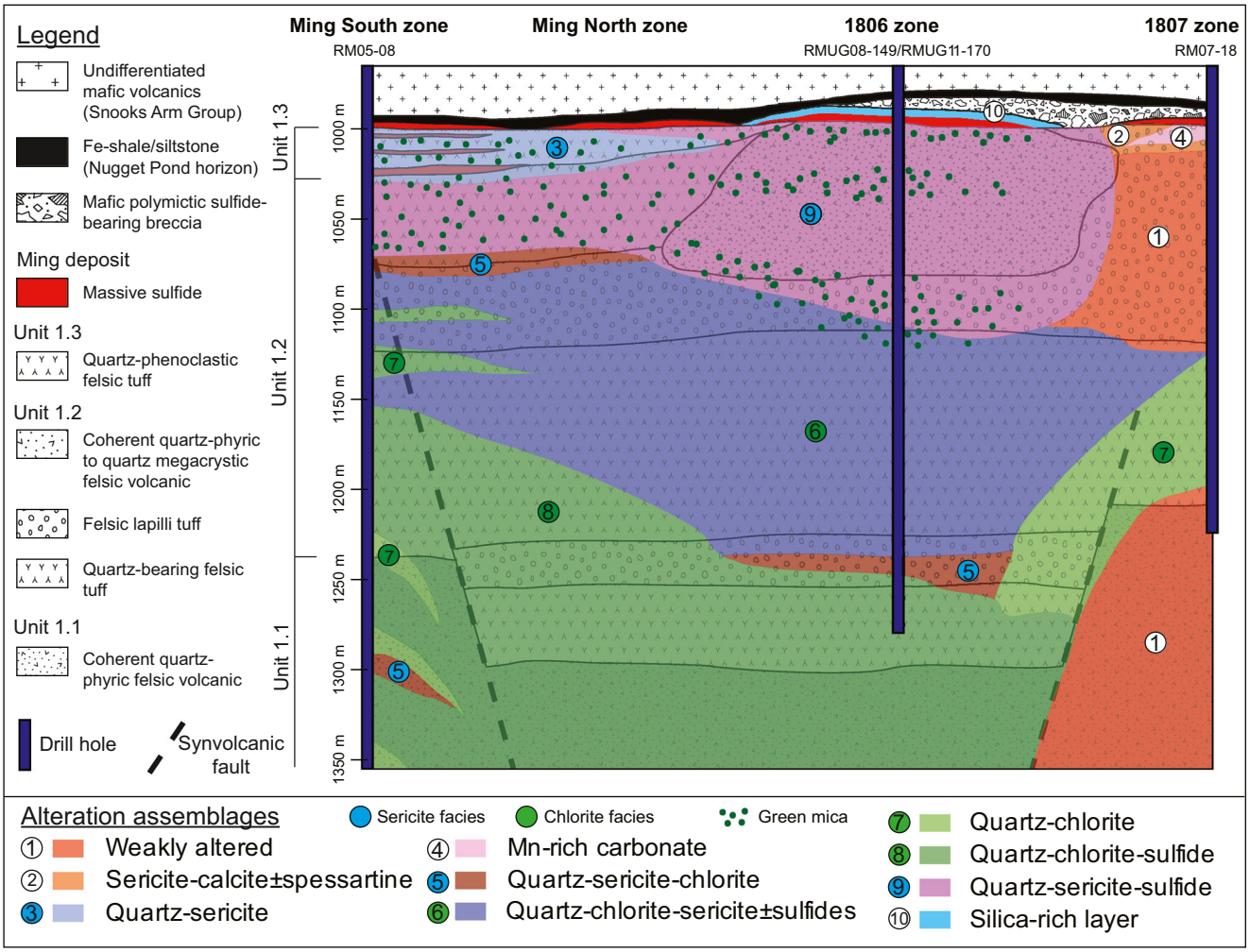

Fig. 4 Schematic reconstruction of the volcanic and volcaniclastic host succession, structural, and alteration assemblages associated with the Ming deposit. The dikes were omitted for clarity. This cross section is constructed based on information collected from representative drill holes, geochemically characterized in detail in Fig. 10 and ESM 1 Figs. 4 and 5. The silica-rich layer locally extends above the 1807 zone (not shown)

(Thompson et al. 1999; Herrmann et al. 2001). A total of 1001 analyses were acquired systematically or selectively on 56 drill holes intersecting different parts of the Ming deposit following the methods outlined in Buschette and Piercey (2016), which are summarized in ESM 2.

Maximum AlOH absorption features vary between 2010 and 2012 nm in less intense alteration assemblages (i.e., least-altered, weakly altered, and sericite–calcite ± spessartine), whereas the values are lower in the most intense alteration assemblages (ESM 1 Fig. 3), regardless of the unit. Lower AlOH absorption values are typically found in the Ming South zone, whereas higher values are restricted to the 1807 and 1806 zones. Maximum FeOH absorption wavelengths are relatively constant throughout the alteration facies, i.e., between 2246.4 and 2254.5 nm, although with a slight increase in chloritic assemblages (ESM 1 Fig. 3). Significantly shorter absorption wavelengths (Fe-poor) were yielded in the quartz–sericite–sulfide and silica-rich layer assemblages.

Mineral chemistry

The compositions of chlorite, mica, calcite, and biotite in 11 samples representative of each alteration assemblage were obtained by electron probe micro analysis (EPMA) for quantitative analyses using a JEOL JXA-8230 EPMA at the Department of Earth Sciences, Memorial University of Newfoundland. The analytical procedures are outlined in ESM 2. Average compositions of minerals for each assemblage are given in ESM 3 Tables 1 to 4.

Chlorite composition

Chlorite compositions are mostly homogenous and Mg-rich with Fe/(Fe + Mg) = 0.35–0.44, plotting within the Mg end-member of the ripidolite field (Fig. 7a; ESM 3 Table 1; Hey 1954). The high-Mg chlorite in the quartz–sericite–sulfide assemblage shows distinctively lower values (~ 0.17) (Fig. 7a).

Sericite composition

The compositional range for the sericite is $(K,Na,Ca,Ba)_{1.58–1.97}(Al,Fe,Mg,Ti,Cr,V,Mn)_{4.08–4.24}Al_{1.58–1.81}Si_{6.19–6.42}(OH)_4$, and thus is muscovitic (e.g., Deer et al. 2013). Sericite in chlorite-rich assemblages has 2.91–4.10 wt% FeO, whereas sericite-rich assemblages closer to the massive sulfides have lower FeO contents (1.36 and 1.82 wt%, respectively; ESM 1 Fig. 3). Sericite forms a continuous array in Fe/(Fe + Mg)–Al space (Fig. 7b), with sericite from the quartz–sericite assemblage having the highest Al values (averaging 36.5 wt%), and those from the sericite–calcite ± spessartine with the lowest values (averaging 32.7 wt%). This range of Al is also consistent with the hyperspectral results where sericite with the highest Al contents has the lowest values in 2200 nm absorption location. The Na_2O content in sericite for most assemblages ranges from ~ 0.5 to 0.7 wt%, except for the quartz–chlorite assemblage, in which values average 1.29 wt% Na_2O. The latter also contains the lowest K_2O, BaO, and MgO (ESM 3 Table 2). The compositions of muscovite porphyroblasts in sericite-rich layers are identical to the surrounding groundmass, indicating that recrystallization from metamorphic overprinting has not changed the signature of the white micas and they reflect the original hydrothermal mica compositions.

The distinctive green micas analyzed in the study ($n = 3$) yielded Cr_2O_3 values up to 0.36 wt% (ESM 3 Table 2) and locally had up to 0.17% V_2O_3 in the Lower Footwall zone and have fuchsite compositions (Deer et al. 2013). Besides Cr_2O_3, there are no other geochemical distinctions between green micas and neighboring sericite.

Calcite composition

Calcite in the Ming deposit has broadly similar FeO and MgO contents in the Mn–Ca-rich and silica-rich assemblages, and both have trace amounts of Zn, Sr, and Ba (ESM 3 Table 3). The MnO content in calcite from the Mn-rich carbonate assemblage (5.32 wt% MnO) below the 1807 zone is significantly higher than that in calcite from the silica-rich layer (0.67 wt% MnO).

Biotite composition

Biotite from Ming is mostly metamorphic in origin, and only a few are of potential primary origin in least-altered rocks. Biotite analyses were predominantly made on variably colored porphyroblasts. Some of the light yellow-brown colored biotite found in the quartz–sericite, quartz–sericite–sulfide, and Mn-rich carbonate assemblages are phlogopitic with high Mg/(Mg + Fe) and Si/Al ratios (Fig. 7c), whereas darker biotite generally has lower Mg/(Mg + Fe) and Si/Al ratios. The BaO content in biotite in the Mn-rich carbonate assemblage is significantly higher than the other assemblages with values averaging 0.64 wt% BaO (ESM 3 Table 4).

Alteration paragenesis

The paragenetic evolution of the Ming hydrothermal system can be established with cross-cutting relationships combined with mineral associations and chemistry (Fig. 8a). The quartz–sericite–chlorite assemblage is interpreted to be the earliest alteration assemblages (stage 1) as it forms isolated lenses between intense chlorite alteration facies (Fig. 4). The spatial association and similar compositions of sericite and chlorite (i.e., similar Fe/(Fe + Mg); Fig. 7a, b) from the quartz–sericite assemblage with quartz–sericite–chlorite assemblage suggest the former is also paragenetically early. The weak alteration and sericite–calcite ± spessartine assemblage are overprinted by the quartz–chlorite assemblage at depth below the 1807 zone and are therefore also interpreted to be paragenetically earlier.

The quartz–chlorite, quartz–chlorite–sulfide, and quartz–chlorite–sericite assemblages cross-cut the sericite-rich assemblages of stage 1 and are themselves cut by younger quartz–sericite–sulfide (stage 3; Figs. 6b, c and 8a). In the case of the Mn-rich carbonate assemblage that cross-cuts the footwall of the 1807 zone, its paragenetic relationship to the chloritic and late quartz–sericite–sulfide is unclear and is considered here as an intermediate stage (stage 2b).

Lithogeochemistry

A suite of 188 samples was collected from drill core and underground workings for lithogeochemistry. Samples were collected to characterize primary and secondary geochemical signatures of the host successions and their spatial distributions. Major and minor elements were obtained by lithium metaborate/tetraborate fusion, followed by HNO_3 dissolution and analyzed by inductively coupled plasma atomic emission spectroscopy (ICP-AES). Trace elements were analyzed using multiacid ($HF–HNO_3–H_3BO_3$) dissolution with a finish by inductively coupled plasma-mass spectrometry (ICP-MS). The analytical and quality assurance and control procedures are described in detail by Pilote and Piercey (2018) and summarized in ESM 2. The average and complete analytical results are available in ESM 3 Tables 5 and 6, respectively.

Primary signatures

Least-altered samples from the Ming deposit host sequence were previously reported in Pilote and Piercey (2018) but are used here as the baseline to assess elemental changes in hydrothermally altered rocks. Except for the silica-rich layer, regardless of the host units and alteration, most samples have subalkalic signatures (Fig. 9a; Winchester and Floyd 1977;

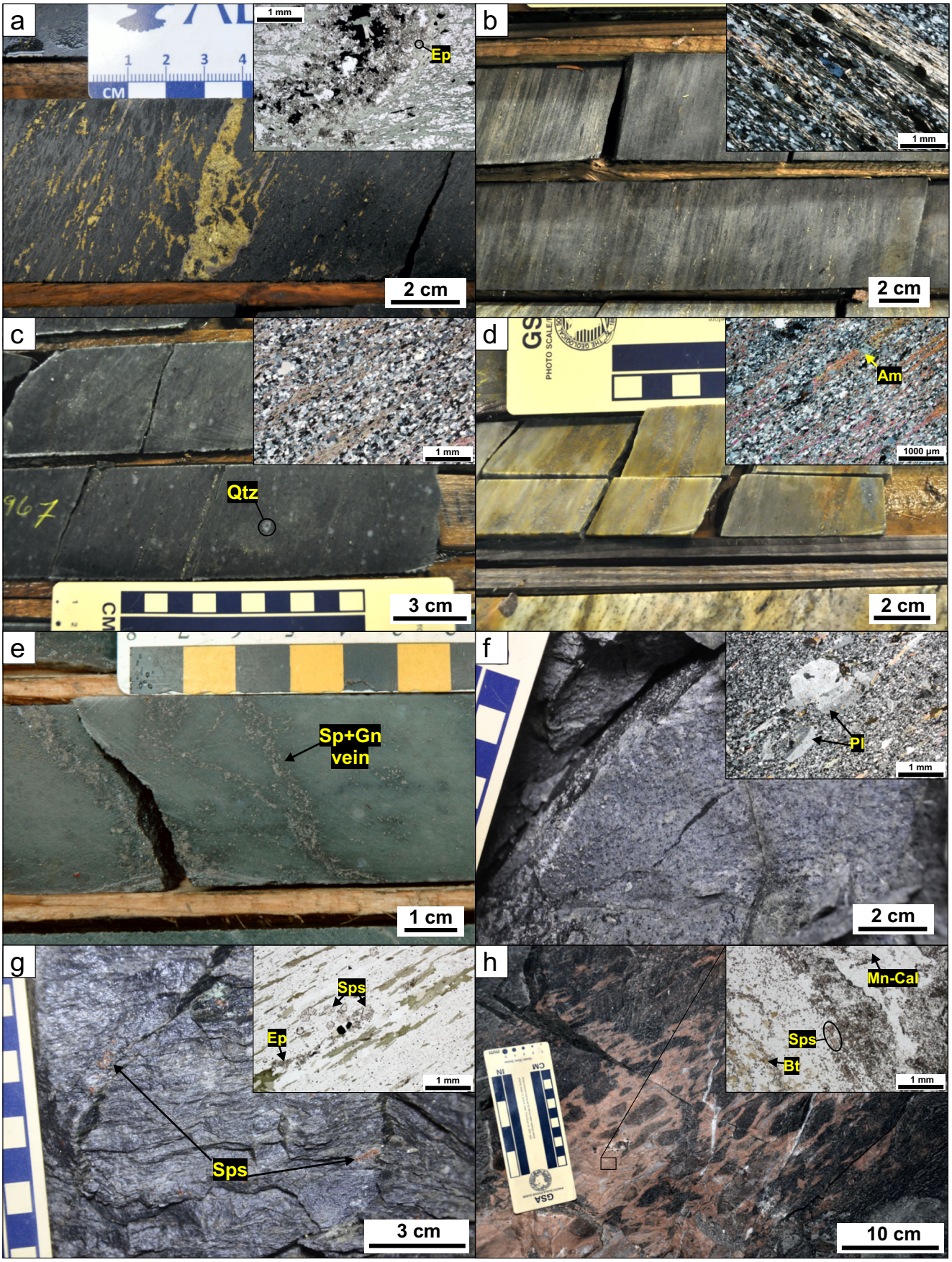
a
1 mm
Ep
2 cm
b
1 mm
2 cm
c
1 mm
Qtz
3 cm
d
Am
1000 µm
2 cm
e
Sp+Gn
vein
1 cm
f
Pl
1 mm
2 cm
g
Sps
Ep
1 mm
Sps
3 cm
h
Mn-Cal
Sps
Bt
1 mm
10 cm

◀ **Fig. 5** Photographs of representative samples of the different alteration assemblages from the Ming deposit. **a** Drill core section representative of the quartz–chlorite–sulfide (chalcopyrite + pyrrhotite) alteration assemblage. Note the light reflection onto the surface enhancing the network of anatomizing chlorite veins (RM06-04e; 1120 m; Lower Footwall/Ming South zones). Inset shows quartz–chlorite–sulfide (chalcopyrite + pyrrhotite)–epidote (Ep) vein in a quartz–chlorite groundmass (sample 62,085; level 1450; Lower Footwall/Ming South zones). **b** Drill core section revealing the pervasive nature of the quartz–chlorite–sericite assemblage (RM04–07; 936 m; Lower Footwall/Ming South zones). Inset shows strong fine-grained quartz–chlorite–sericite alteration assemblage (sample 36,636; RMUG11-170; 130 m; Lower Footwall/1806 zones). **c** Drill core section representative of the quartz–sericite–chlorite assemblage with relic quartz (Qtz) phenocrysts. Inset shows polarized light photomicrographs of the quartz–sericite–chlorite assemblage. Note the coexisting sericite and chlorite developed as layers in a fine-grained quartz-rich matrix (sample 62,064; RM04-04; 1087 m; Ming South zone). **d** Representative drill core photo of the quartz–sericite alteration assemblage with sulfide-rich veins transposed onto S_2 fabrics (RM04-04; 893.0 m; Ming South zone). Inset shows the strong and pervasive quartz–sericite alteration. Amphibole (Am) porphyroblasts developed onto sericitic layers (sample 62,057; RM04-04; 893.0 m; Ming South zone). **e** Drill core section representative of the quartz–sericite–sulfide assemblage with associated sphalerite (Sp)–galena (Gn)-rich veins (RMUG08-145; 20 m; 1806 zone). **f** Representative least-altered rhyodacite. Note the pervasive light green epidote alteration and metamorphic fabric defined by biotite (level 469; 1807 zone). Inset shows relic plagioclase (Pl) phenocrysts in a fine-grained quartz–plagioclase ± sericite groundmass (sample 62,081; level 469; 1807 zone). **g** Representative outcrop of the sericite–calcite ± spessartine with spessartine (Sps) glomeroporphyroblasts on well-developed foliation (level 329; 1807 zone). Inset shows polarized light photomicrograph of the sericite–calcite ± spessartine (Sps) assemblage (sample 60,507; level 329; 1807 zone). Some epidote (Ep) also developed in this assemblage. **h** Outcrop-scale example of the Mn-rich carbonate alteration assemblage cross-cutting the weakly altered assemblage (level 481; 1807 zone). Inset shows a Mn-rich calcite (Mn-Cal), spessartine (Sps), and biotite (Bt) assemblage developed in the 1807 zone (sample 62,199; level 481; 1807 zone

Pearce 1996) and dacitic to rhyodacitic compositions (Fig. 9b; Winchester and Floyd 1977; Pilote and Piercey 2018). Most samples cluster along a single slope that intersects the origin in Al_2O_3–Zr space (Fig. 9c), typical of cogenetic rocks that have been affected by mass and/or volume change associated with alteration (Barrett and MacLean 1994). The samples have calc-alkalic Th/Yb (~ 5) and Zr/Y (~ 10) values (Fig. 9d; Ross and Bédard 2009), although unit 1.3 is slightly more enriched than units 1.1 and 1.2. On an extended primitive mantle-normalized plot, the least-altered rocks show light rare earth elements (LREE) enrichment relative to the heavy rare earth elements (HREE) (Fig. 9e), with negative Nb anomalies typical of arc magmas (e.g., Pearce et al. 1995). The samples are generally depleted in trace elements (e.g., Zr < 80 ppm; ESM 3 Table 5) and have low Yb_{cn} (cn = chondrite normalized) values and high $(La/Yb)_{cn}$ ratios and have FI- and FII-types affinities (Fig. 9f). These latter geochemical attributes are products of deep level (> 15 km), garnet/amphibole controlled, and low temperature (~ 700–800 °C) partial melting (Lesher et al. 1986; Hart et al. 2004; Pilote and Piercey 2018).

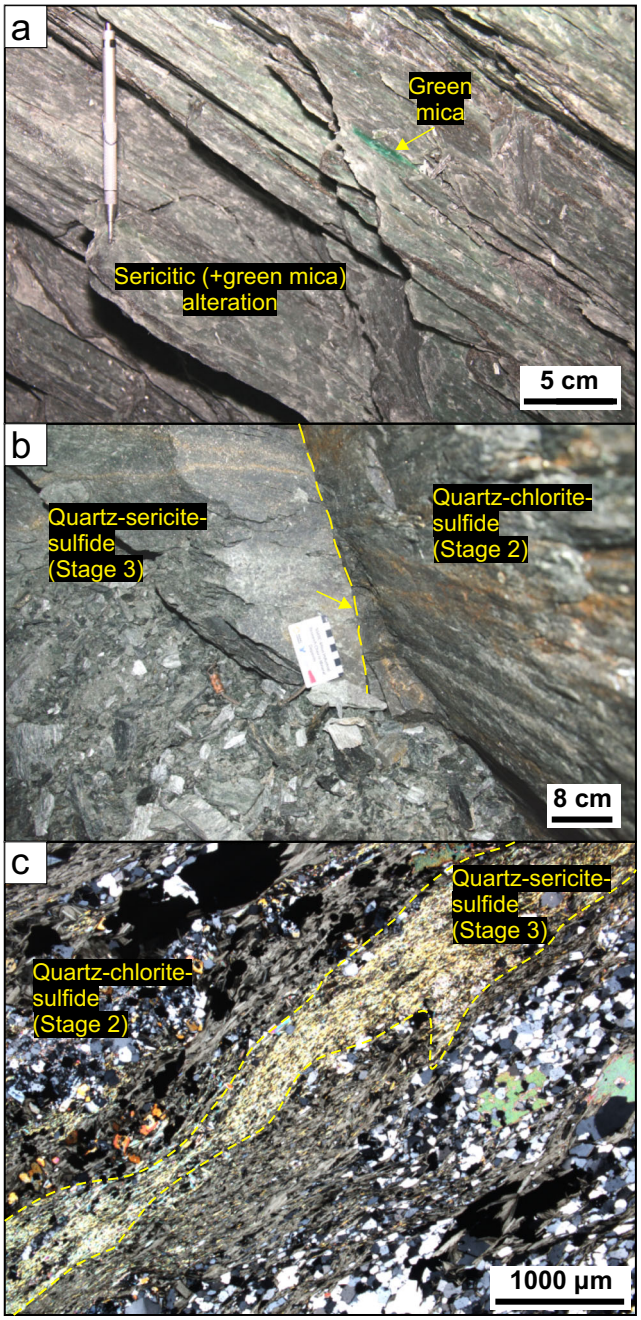

Fig. 6 Underground and drill core photos and photomicrographs. **a** Distinctive green mica developed within a sericitic assemblage (level 103; 1806 zone). **b**, **c** Relationship between the quartz–sericite–sulfide and quartz–chlorite(–sulfides) assemblages. **b** Sharp primary contact (yellow arrow) between the two assemblages (level 1450; Lower Footwall zone). **c** Photomicrograph showing the chloritic groundmass overprinted by a sericitic vein, belonging to the quartz–sericite–sulfide assemblage. This sample was collected on the right wall in **b** (sample 103,413; level 1450; Lower Footwall/1806 zones)

All features above suggest that the felsic rocks from Ming are cogenetic. However, while units 1.1 and 1.2 are similar geochemically despite their lithofacies differences (Pilote et al.

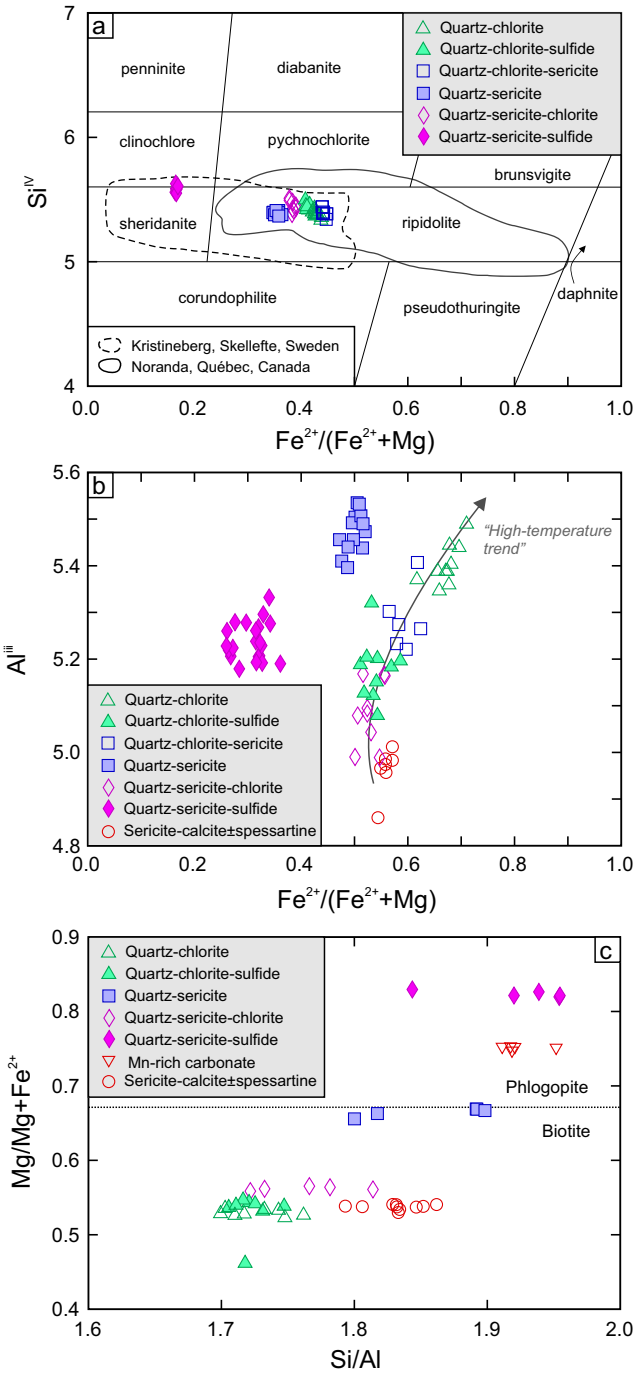

Fig. 7 Composition of chlorite in the Ming alteration assemblages. **a** Hey diagram showing chlorite compositions of the Ming deposit in the ripidolite, sheridanite, and clinochlore fields. Also shown are the range of chlorite compositions from Noranda (Hannington et al. 2003b) and Kristineberg area, Skellefte Group (Hannington et al. 2003a). The chlorite from Ming are generally low in Fe/(Fe + Mg) ratios, comparable to the ones from the Kristineberg area, which likely reflect the low temperature nature of the seawater-saturated volcaniclastic piles of units 1.2 and 1.3. **b** Al vs. Fe/(Fe + Mg) diagram showing compositions of sericite. The trend in the data is interpreted to reflect chlorite abundance and conditions at higher temperatures than the sericitic assemblages. **c** Mg/(Mg + Fe) vs. Si/Al diagram showing compositions of biotite. The division between phlogopite and biotite (Mg:Fe = 2:1) is from Deer et al. (2013)

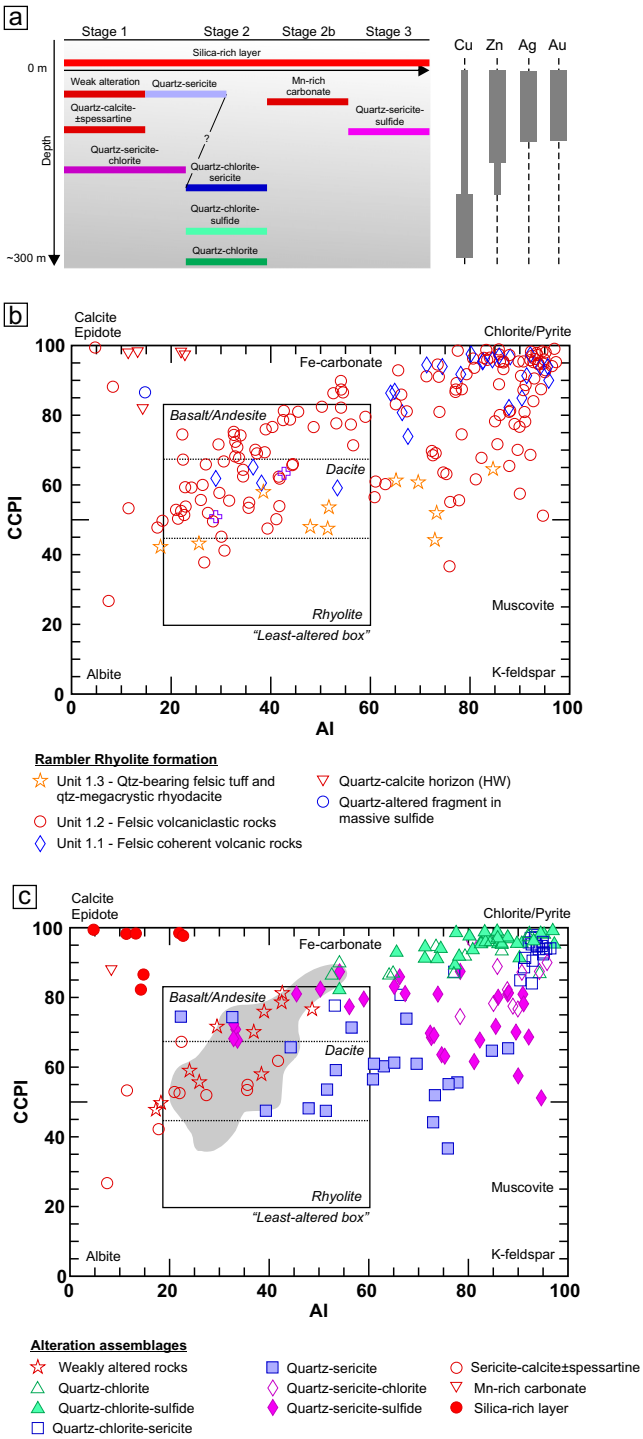

Fig. 8 **a** Paragenetic evolution of the alteration assemblages in relation to depth (approximate scale). Three main stages of hydrothermal alteration have been established for the Ming deposit. The paragenetic relationship between some alteration assemblages is not well constrained, although the overall evolution of the hydrothermal system is consistent with the well documented paragenetic relationships. **b** Alteration box plot showing all samples and categorized based on the units rather than alteration assemblages (modified from Large et al. 2001b). **c** Distribution of alteration assemblages. In gray is the distribution of least-altered samples, based on the criteria set by Pilote and Piercey (2018). AI alteration index (Ishikawa et al. 1976), CCPI chlorite–carbonate–pyrite index (Large et al. 2001b)

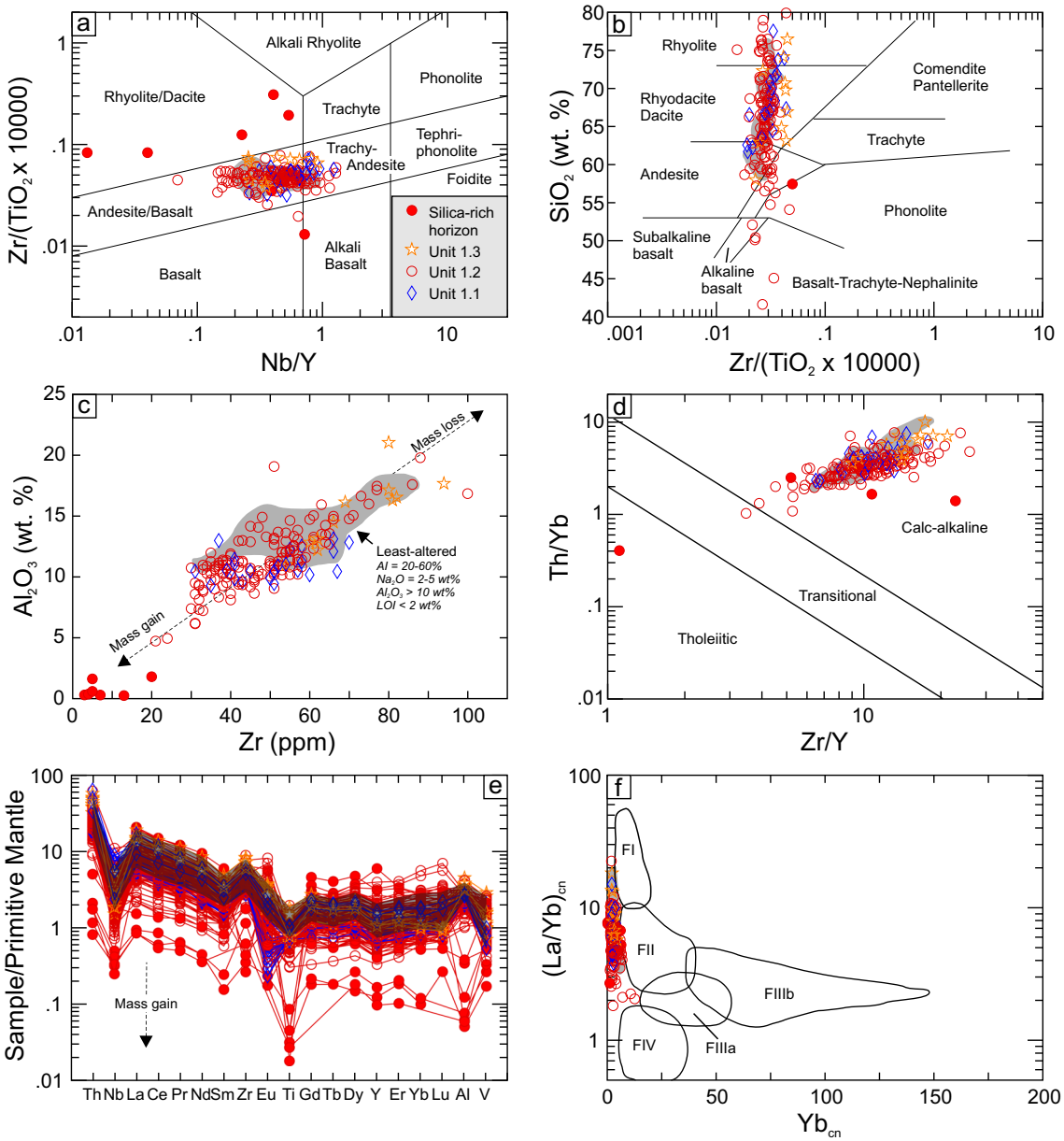

Fig. 9 Petrochemical affinity of all analyzed samples from the Rambler Rhyolite formation. **a** Zr/TiO_2 vs. Nb/Y discrimination diagram from Winchester and Floyd (1977), revised by Pearce (1996). **b** Zr/TiO_2 vs. SiO_2 discrimination diagram from Winchester and Floyd (1977). **c** Al_2O_3 vs. Zr. **d** Th/Yb vs. Zr/Y discrimination diagram from Ross and Bédard (2009). Fields in gray are least-altered rocks as defined by Pilote and Piercey (2018). **e** Primitive mantle-normalized extended element diagram. **f** Chondrite-normalized $[La/Yb]_{cn}$ vs. Yb_{cn} discrimination diagram from Lesher et al. (1986) and Hart et al. (2004). The fields (FI-FIV) proposed by the latter authors are used to identify fertile vs. infertile felsic volcanic rocks to host mineralization, with FIII and FIV being the most prospective. Chondrite and primitive mantle normalizing values are those of Nakamura (1974) and Sun and McDonough (1989), respectively

2017), unit 1.3 is slightly more enriched in trace elements, so for simplicity and for alteration and mass balance calculations, units 1.1 and 1.2 are amalgamated hereafter as one single geochemical unit, separate from unit 1.3 (ESM 3 Table 5).

Alteration composition

On alteration box plots (Large et al. 2001b), samples from units 1.1/1.2 trend towards the (Fe-rich) chlorite/pyrite node, whereas samples from unit 1.3 trend towards the muscovite node (Fig. 8b). Alteration assemblages at Ming have chemical signatures that mirror their alteration mineralogy (Fig. 8c), with weakly altered rocks overlapping the least-altered field; the Mn-rich carbonate assemblage and silica-rich layer plot near the Ca-rich (epidote/calcite) node; some samples from the sericite–calcite ± spessartine assemblage that show Na-enrichment (albitization) lie near the albite node; and the chlorite–sulfide-rich assemblages plot near the pyrite–chlorite node

(Fig. 8c). In the case of the quartz–sericite and quartz–sericite–sulfide assemblages, although spatially proximal, they record distinct compositional trends (Fig. 8c): both form negative linear arrays towards the muscovite (K-rich) node, but the quartz–sericite–sulfide assemblage shows systematically higher carbonate–chlorite–pyrite index (CCPI) values (Fig. 8c).

A representative chemostratigraphic section constructed from drill holes that intersect the Ming South zone is shown in Fig. 10. Other sections for the 1807 and 1806 zones are in ESM 1 Figs. 4 and 5, respectively. These provide a spatial representation of various geochemical and spectral responses relative to the ore zones. Intersections with greater chlorite abundances show low mobile and immobile elements, with the exception of Cr, whereas the opposite is shown in the sericitic assemblages. Copper and Zn values are the highest in the chlorite-rich and sericite-rich assemblages, respectively. Lower alteration intensities are reflected by lower alteration indices (AI and CCPI) and Mg#. The Ba/Sr ratios and Eu/Eu* values are generally the highest near the massive sulfide lenses. Moreover, variations in the 2200 nm and 2250 nm absorption ranges are notable with both features increasing near the sulfide lenses.

Some of the spatial trends in the chemostratigraphic sections are also replicated when plotted against alteration index (AI) and illustrate key elemental behavior in response to various alteration intensities (Fig. 11). Barium is predominantly depleted in the quartz–chlorite–sulfide and quartz–chlorite assemblages, whereas Sr progressively decreases with increasing intensity of alteration, regardless of the assemblage (Fig. 11a, b). The low values in Ba and Sr in the silica-rich layer are likely due to the lack of feldspars (Fig. 11a, b). The MnO content is high in the Mn-rich carbonate, and sericite–calcite ± spessartine assemblages, consistent with the abundance of Mn-rich minerals, is variable in the sericitic assemblages, whereas it virtually remains constant throughout the weakly altered rocks and chloritic assemblages (Fig. 11c). Arsenic, Sb, Pb, Zn, and Hg are generally higher in the quartz–sericite and quartz–sericite–sulfide assemblages near the massive sulfide lenses, whereas, as previously mentioned, Cu is mostly associated with the chloritic assemblages at depth (Fig. 11d–i). In the footwall rocks, the latter metals are hosted in quartz–sulfide-rich stringer veins, in which As, Sb, Pb, Zn, and Hg are found in veins predominantly composed of arsenopyrite, sphalerite, sulfosalts, and tellurides and Cu in chalcopyrite-rich veins.

Mass balance and elemental gains and losses

Absolute elemental changes associated with alteration were calculated using the isocon technique described in Grant (1986). The calculated relative mass changes are plotted as histograms in ESM 1 Fig. 6.

Most assemblages show a net gain in mass, except for the quartz–sericite assemblage located below the sulfide lenses (Fig. 12d). The relative mass change in SiO_2 mimics the net mass changes in most assemblages, which highlights the role of silica during hydrothermal alteration. All assemblages exhibit elevated loss-on-ignition (LOI), and Na_2O depletions, with the exception of the sericite–calcite ± spessartine assemblage in unit 1.3, which has Na_2O addition (albitization) (Fig. 12c; ESM 1 Fig. 6g). Manganese (MnO), CaO, P, and Y additions mostly occur in the sericite–calcite ± spessartine (of units 1.1/1.2) and Mn-rich carbonate assemblages (Fig. 12b, e). Narrow calcite veinlets in the weakly altered rocks can explain the CaO addition (Fig. 12a). The MgO gains are predominant in chloritic assemblages (Fig. 12g, h), whereas chlorite–barren assemblages are generally depleted in MgO (Fig. 12b–d, i). Similar trends occur with Fe_2O_{3t}, although the addition of Fe in the quartz–sericite–sulfide assemblage reflects its high sulfides contents (Fig. 12i). The quartz–sericite, quartz–sericite–chlorite, and quartz–sericite–sulfide assemblages show significant gains in K_2O (Fig. 12d, f, i), whereas losses are shown in all other assemblages. Transition metals Ni and Cr are added in most assemblages, except in the Mn-rich and quartz–sericite–chlorite assemblages (Fig. 12b, c, e, f). Copper, Zn, and Ag are added to various assemblages reflecting the varying abundances chalcopyrite, sphalerite, and Ag-bearing minerals in the alteration assemblages.

Discussion

Hydrothermal alteration architecture and volcanic controls

Alteration is limited to the footwall rocks of the Ming deposit (Fig. 4). Most of the intense chlorite facies alteration (quartz–chlorite, quartz–chlorite–sulfide, and quartz–chlorite–sericite) occurs at depth at or near the coherent–volcaniclastic interface of units 1.1 and 1.2, between 300 and 50 m below the massive sulfides. A gap of < 100 m separates the chloritic assemblages from the massive sulfide-bearing interval that consists of sericite- and Mn-rich carbonate assemblages. The deep, laterally restricted, and linear distribution of the alteration within the Rambler Rhyolite reflects controls by synvolcanic structures and focusing of hydrothermal fluid discharge (Large 1992). Furthermore, recent work has demonstrated that the involvement of synvolcanic faults was critical in the development of the Ming deposit by controlling the extent and geometry of felsic volcaniclastic-dominated units 1.2 and 1.3 and providing permeable, planar, and restricted pathways to hydrothermal fluids (Pilote et al. 2017). The elongated shapes of the ore zones are thus attributed to the controlling effect of these parallel

Fig. 10 Chemostratigraphic profile of drill hole RM05-08, representative ▶ of the Ming South zone. Horizontal lines represent location of analyzed host rock samples. Bar plots for Cu and Zn (wt% scale; identified in the central part of the profile) represent assay data provided by Rambler Metals and Mining Ltd. AI alteration index (Ishikawa et al. 1976), CCPI chlorite–carbonate–pyrite index (Large et al. 2001b), UL upper lens, LL lower lens

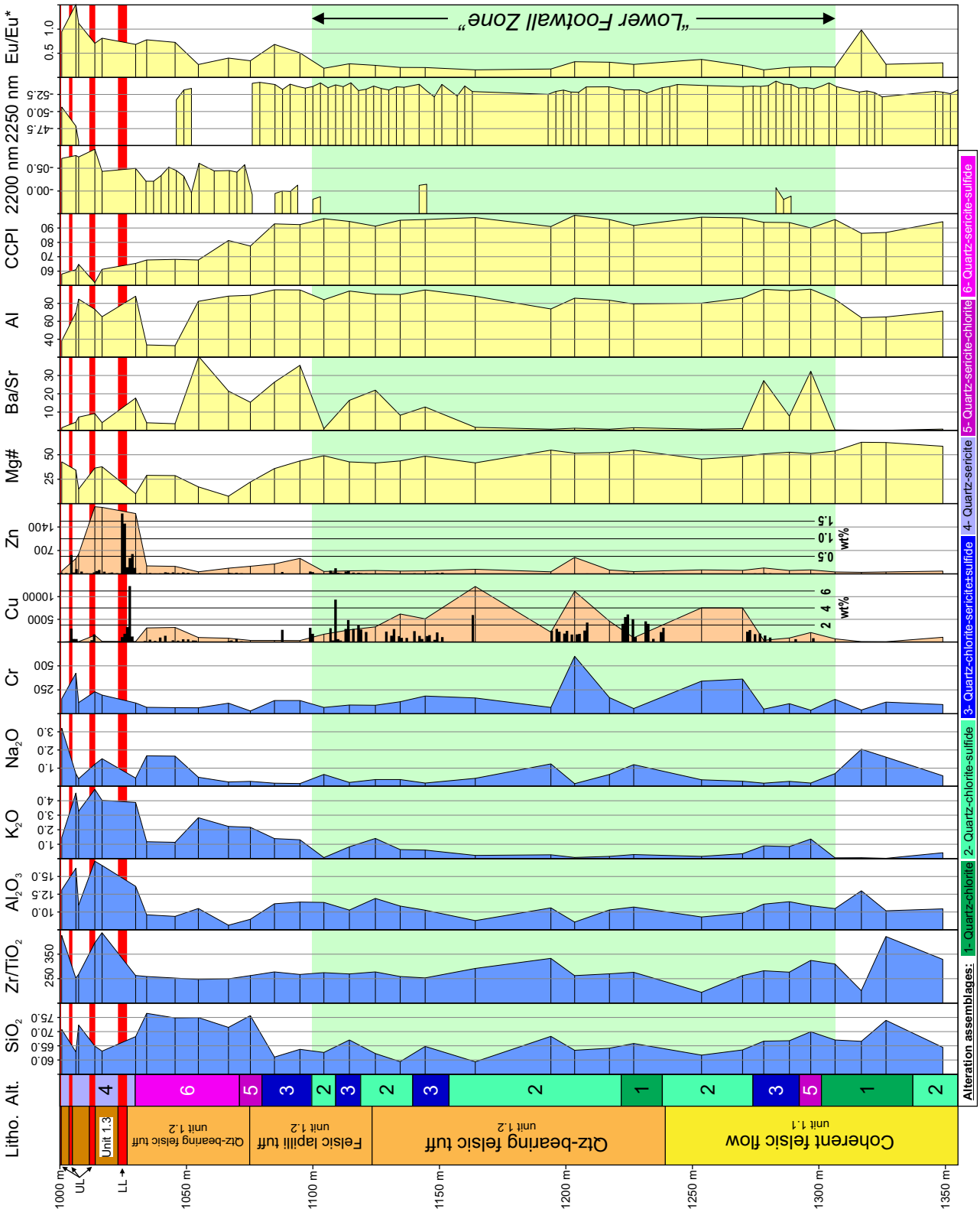
Litho.
Alt.
SiO2
Zr/TiO2
Al2O3
K2O
Na2O
Cr
Cu
Zn
Mg#
Ba/Sr
Al
CCPI
2200 nm
2250 nm
Eu/Eu*
"Lower Footwall Zone"
Coherent felsic flow
unit 1.1
Qtz-bearing felsic tuff
unit 1.2
Felsic lapilli tuff
unit 1.2
Qtz-bearing felsic tuff
unit 1.2
Unit 1.3
UL
LL
1000 m
1050 m
1100 m
1150 m
1200 m
1250 m
1300 m
1350 m
wt%
Alteration assemblages:
1- Quartz-chlorite
2- Quartz-chlorite-sulfide
3- Quartz-chlorite-sericite±sulfide
4- Quartz-sericite
5- Quartz-sericite-chlorite
6- Quartz-sericite-sulfide

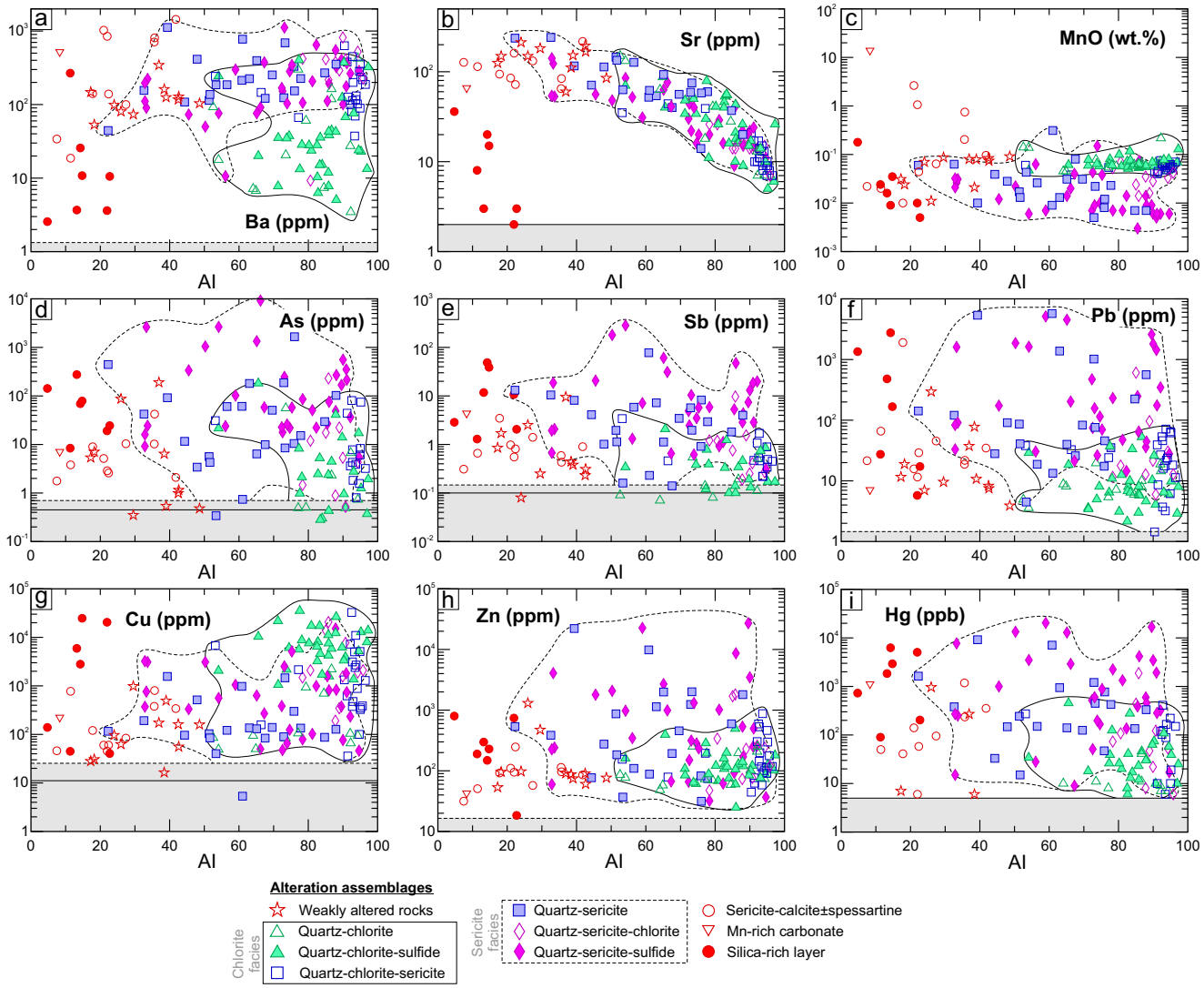

Fig. 11 Alteration index (AI; Ishikawa et al. 1976) vs. **a** Ba, **b** Sr, **c** MnO, **d** As, **e** Sb, **f** Pb, **g** Cu, **h** Zn, and **i** Hg for altered felsic rocks from the Ming deposit, showing the variations in trace elements and metals with increasing degree of alteration. The gray fields represent the lower detection limit, with the average values as solid lines, and the upper 2σ as dashed lines

synvolcanic structures and the disposition of the quartz–chlorite–sulfide assemblage (or Lower Footwall zone) at depth supports this (Pilote et al. 2017).

Although the location of some fluid discharge may have been controlled by synvolcanic faults, the vertical distribution and variation of the alteration assemblages were also controlled by other factors. For example, many of the alteration assemblages are conformable to semi-conformable to stratigraphy and some preferentially associated with certain types of lithofacies, suggesting a lithological control on fluid circulation (Fig. 4). In addition, the chlorite alteration facies in the Ming deposit is generally restricted to the deeper parts of the Rambler Rhyolite formation, whereas the sericite alteration facies is located in the upper parts of the formation (Fig. 4). In VMS systems, it is widely accepted that chlorite alteration forms due to the reaction of high-temperature (> 300 °C), slightly acidic (pH ≈ 4–5) fluids with surrounding rocks, whereas sericitic alteration is attributed to cooler (< 200 °C) and more acidic (pH < 4) fluids (Walshe and Solomon 1981; Schardt et al. 2001). In the Ming deposit, the alteration distribution suggests that the fluids that altered the upper part of the formation were of lower temperature and pH. It is also possible that this may be partly due to the permeability of units 1.2 and 1.3 at the time of their accumulation, as opposed to coherent felsic volcanic rocks of unit 1.1, which led to greater fluid–rock interaction and intensity of alteration (Large 1992; Gibson et al. 1999) and is partly supported by the presence of chlorite- and Cu-rich mineralization in the Lower Footwall zone (Lydon 1988, 1996) vs. sericite–quartz and Zn–Pb–sulfosalt-rich mineralization in the massive sulfide lenses.

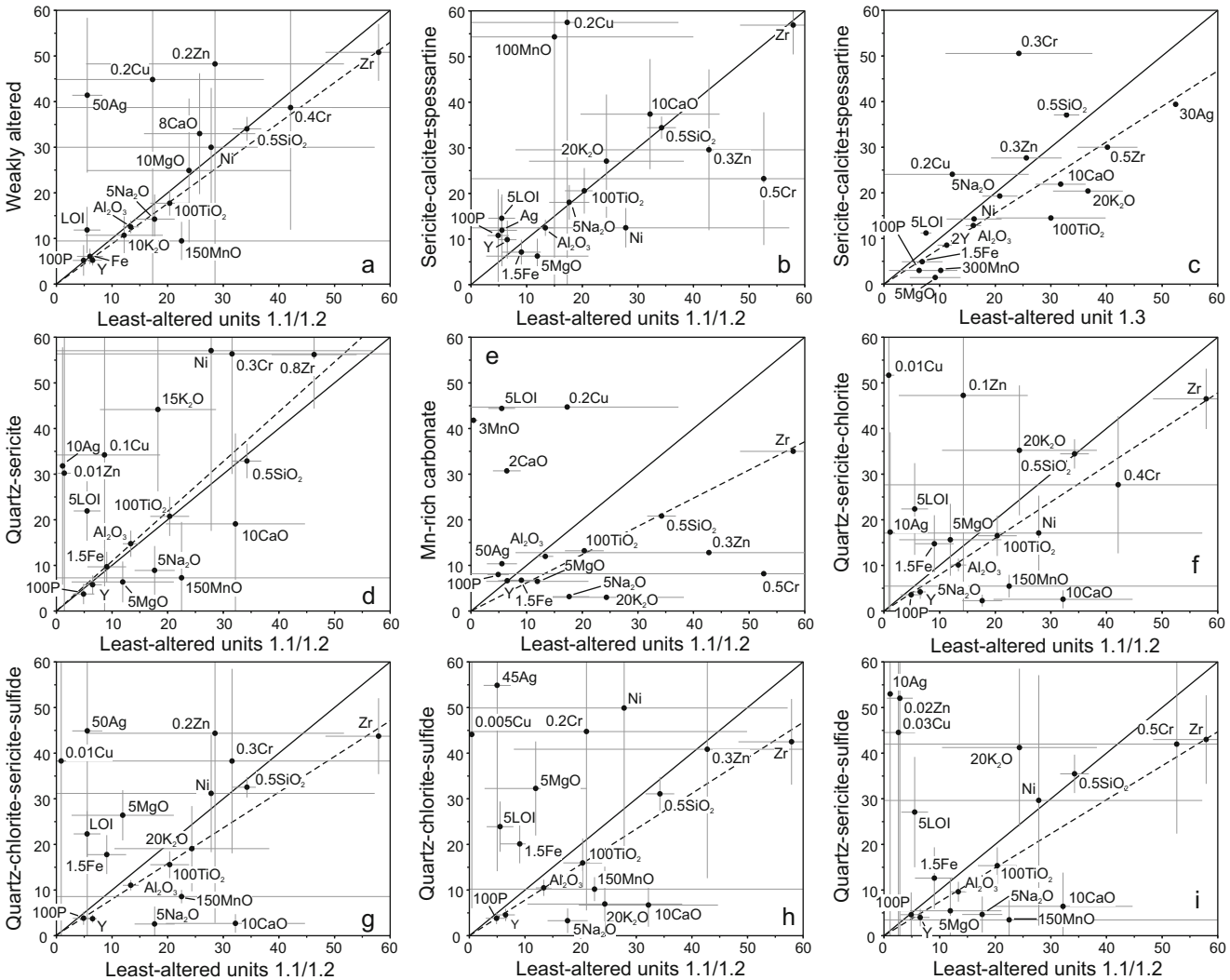

Fig. 12 Best-fit isocon diagrams showing compositional changes during alteration (modified from Grant 1986). The dashed line represents the best fit isochon based on elements that are considered immobile or the least-mobile during alteration (Al, Ti, Zr). Volume loss will shift the isocon above the 1:1 reference (solid) line and a volume gain, below. Elements that fall above the isocon were hydrothermally added; those that fall below were removed. Except for **c**, all diagrams are compared to the least-altered rocks of the combined units 1.1 and 1.2. In **c**, the respective alteration assemblages are compared to the least-altered rocks of unit 1.3. Each element is subjectively scaled to visually emphasize changes in components that could otherwise be underestimated. The accompanying horizontal and vertical lines indicate the 1σ error for each element. The propagation of errors follows the method of Huston (1993)

Major element associations and processes

The major and trace element geochemistry in the alteration footprint of VMS deposits reflects the physicochemical nature of the fluids, host rock chemistry and permeability/porosity, and intensity of fluid–rock interaction (Lydon 1988, 1996). In the Ming deposit, the observed losses in Na, K, Ba, and Sr (Figs. 10 and 11a, b; ESM 1 Figs. 4 and 5; ESM 3 Table 5) associated with intense chlorite alteration, coupled with the addition of K, Mg, and Fe, reflect the destruction of feldspar and formation of sericite (K) and/or chlorite (Mg–Fe). These elemental changes are common in VMS systems as hydrothermal fluids interact with host rocks during fluid–rock reaction, such as ion exchange/substitution and/or hydrolysis (Reed 1997). In particular, hydrolysis or breakdown of feldspars is accompanied by a loss of Na^+ coupled with K^+ fixation during sericite formation (K_2O gains) (Fig. 13a). At higher temperatures (> 300 °C), Mg^{2+} and Fe^{2+} in descending seawater are mostly fixed in chlorite and some in micas (Fig. 13b). The resulting fluids have low pH (as the product from the reaction releases H^+; Hajash and Chandler 1982) and are capable of carrying significant metals in solution, explaining the association of chlorite ± sericite alteration with metal enrichment (Lydon 1988, 1996).

Interestingly, as K_2O continues to decrease towards chlorite-rich zones, Na_2O progressively increases towards the most intense alteration (Fig. 13a). This is supported by a number of chlorite analyses in the quartz–chlorite–sulfide

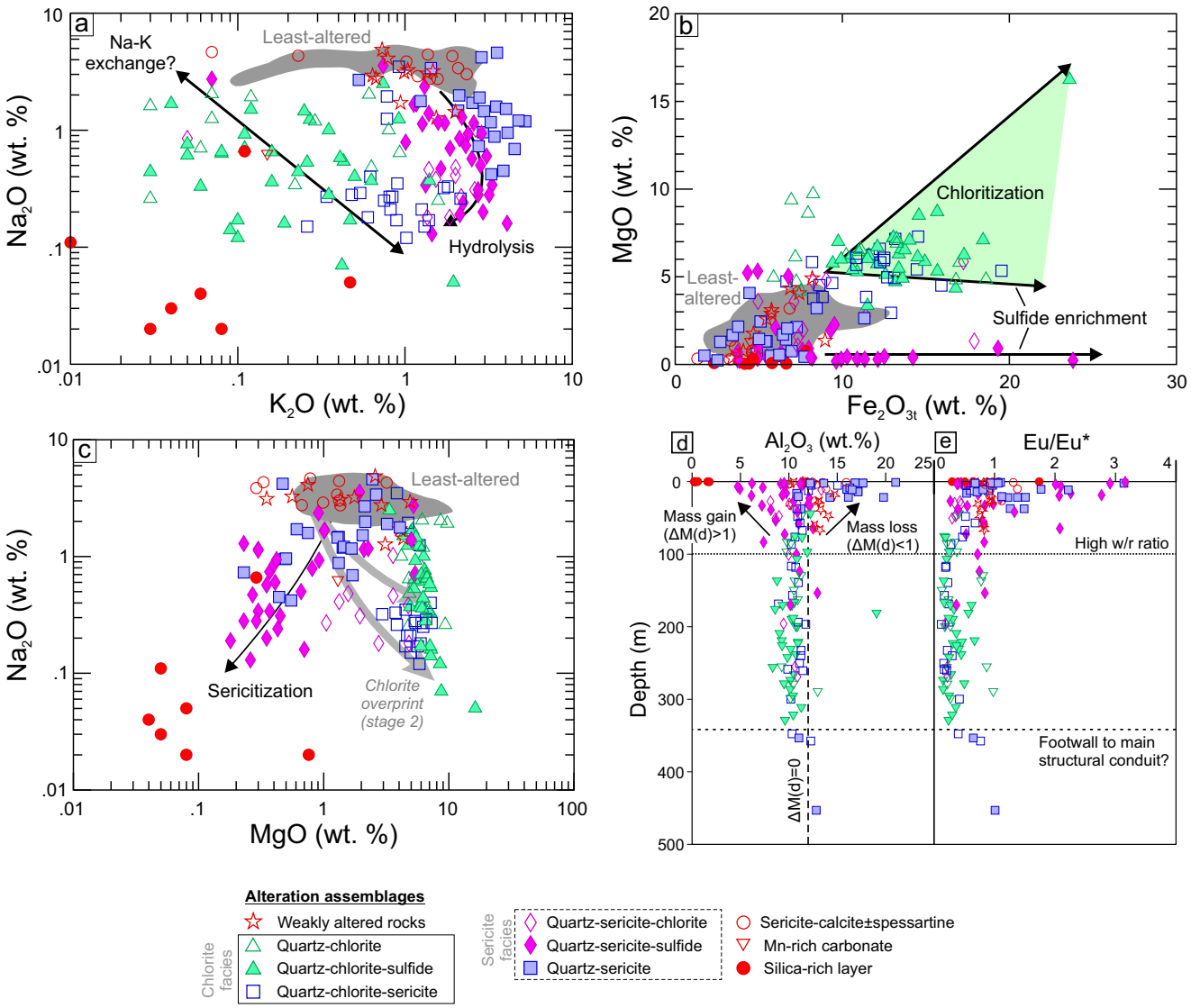

Fig. 13 Variation diagrams illustrating geochemical behavior for variably altered rocks from the Ming deposit. **a** K_2O vs. Na_2O. **b** Fe_2O_{3t} vs. MgO. **c** MgO vs. Na_2O. **d**, **e** Variation diagrams illustrating the variability of Al_2O_3 and Eu/Eu* in relation to depth, respectively. Depth has been normalized to the base of the uppermost massive sulfide lens or the felsic-hanging wall interface. Samples from the overlying silica-rich layer and silica-rich fragments were plotted on the 0 m mark for the sake of simplification

assemblage that yielded anomalous Na_2O content (ESM 3 Table 1). This relationship is uncommon as most VMS deposits show significant depletion to complete absence in Na_2O at their core (Spitz and Darling 1978; Gemmell and Large 1992; Large et al. 2001a-c). Whereas it is common for some deposits to undergo a Na–Mg enrichment as the system heats up and/or cools down (Galley 1993), the negative correlation that exists between Na_2O and MgO (Fig. 13c) makes this an unlikely process. To explain the increase in Na/K ratio, one could envisage two possible scenarios. The first involves influx of Na-rich fluids from the breakdown of plagioclase in the volcanic successions at the base of the hydrothermal system or by a late flux of unmodified seawater (Date et al. 1983). The second scenario involves a phase separation in the hydrothermal fluids from adiabatic boiling where NaCl-rich brine with density greater than its vapor phase would begin to separate at depth (Arnórsson et al. 2007; Monecke et al. 2014). The latter implies that the ascending fluids evolved along the boiling curve in the H_2O–NaCl system and became increasingly saline as the vapor was lost during boiling; hence, increasing the possibility for Na sorption in the chloritic assemblages. Moreover, the presence of Au–Ag enrichment, sulfosalt-rich mineral assemblages, and epithermal suite element enrichments (Hg, As, Sb, Bi, Te) in the ores in parts of the Ming deposits (1806 zone) are consistent with magmatic fluid involvement in deposit genesis (Brueckner et al. 2016) and could partly explain the Na-enrichment present in some of the high-temperature alteration zones in the Ming deposit.

Apart from the silica-rich layer, Ca- and Mn-enrichment is limited to the outer edge of the 1807 zone (Fig. 4), within 10 m

of the massive sulfide. This enrichment is associated with the pervasive quartz–calcite ± spessartine assemblage and the Mn-rich carbonate veining network. Carbonate minerals have a retrograde solubility at fixed pH and partial pressure of CO_2 (Krauskopf and Bird 1995); dissolved Ca and CO_2 from the low temperature seawater likely precipitated instantly as Mn-rich calcite at the contact with ascending hot, Mn-rich hydrothermal fluids. The restricted distribution at the fringe of the Ming deposit marks the outer limit of the hydrothermal convection cell that formed mineralization, which is consistent with what has been seen in other deposits (Herrmann and Hill 2001; Large et al. 2001c; Mercier-Langevin et al. 2014).

Alteration geochemistry in relation to depth: Insight on fluid controls

The relationships between depth in the deposit and key geochemical attributes of the hydrothermal alteration are examined in Fig. 13 d and e. This approach provides a more accurate representation of geochemical behavior on the deposit and overcomes local drill hole to drill hole variations (e.g., Fig. 10), while providing insight into fluid–rock interaction.

Aluminum is an effective element for calculating mass change associated with alteration at Ming. In Fig. 13d, the abundance of Al_2O_3 provides spatial context to these mass changes, with only the upper ~ 100 m of the host successions demonstrating strong variations in Al_2O_3 content, whereas the lower 400 m shows near constant values, regardless of the alteration assemblages. The wide variation in mass that is restricted to the upper section of the deposit is attributed to the greater permeability of the volcaniclastic units 1.2 and 1.3, which enabled greater fluid–rock reaction and by association greater mass changes and Al_2O_3 variability. However, clear divergent patterns are notable near the massive sulfides among the quartz–sericite and quartz–sericite–sulfide assemblages, with an increase and decrease in Al_2O_3 values, respectively (Fig. 13d). As demonstrated by the mass change calculations, the bulk Al_2O_3 content is controlled by the addition or loss in SiO_2. Because the early quartz–sericite assemblage shows an increase in Al_2O_3, or a loss in SiO_2, the fluids were evidently more efficient in flushing out Si then the late quartz–sericite–sulfide assemblage. Furthermore, loss in Si may have contributed in the formation of the silica-rich layer above the 1806 zone.

The marked increase in positive Eu/Eu* anomalies in the sericitic assemblages (Fig. 10; ESM 1 Fig. 5; ESM 3 Table 5) is restricted to the uppermost section of the deposit (Fig. 13e), implying that the enrichment of divalent Eu (Eu^{2+}) occurred within ~ 100 m from the massive sulfides. Also, the highest positive anomalies (Eu/Eu* > 1.5) are found exclusively in the 1806 zone. The solubility of divalent Eu is the greatest in weakly acidic fluids that exceed 250 °C (Sverjensky 1984) and the availability for fluids to transport Eu^{2+} likely depends on the destruction of REE-bearing minerals such as apatite and feldspars. Disequilibrium from the mixing of these Eu^{2+}-enriched fluids with seawater-saturated volcaniclastic rocks could explain the increase in Eu/Eu* values near the massive sulfides. Furthermore, because the enrichment in Eu^{2+} is significantly more important in the 1806 zone implies that cooling of fluids was more significant in the latter zone than the rest of the deposit, suggesting this part of deposit was directly in contact with seawater.

Lithofacies relationships to mineralization and possible controls on metal distribution

The origin of precious metal enrichment in the Ming deposit has been subject to debate; however, recent work has illustrated that the mineralization is associated with syngenetic VMS activity and magmatic fluid involvement (Brueckner et al. 2014, 2016; Pilote et al. 2016). Zinc, Ag, and Au are co-enriched in the paragenetically late quartz–sericite–sulfide assemblage and reflect elevated sphalerite, electrum, and Ag-bearing sulfosalts associated with this assemblage (Brueckner et al. 2014, 2016). Metal grades in the massive sulfides vary within and between lenses and their distribution correlate with the underlying lithofacies; parts that are elevated in Zn, Au, and Ag grades are immediately underlain by coherent felsic volcanic rocks (Pilote et al. 2017). A similar enrichment is also present at the base of these coherent rocks (ESM 1 Fig. 5). The low-permeability of this lithofacies likely acted as a hydrological cap to the ascending fluids, thus preventing the dissipation of the precious metal-bearing fluids into permeable volcaniclastic rocks; a process akin to many capped VMS deposits worldwide (Doyle and Allen 2003; Hannington et al. 2005) and known to be conducive to their enrichment (Piercey et al. 2015).

Proposed model of formation and possible heat source

The massive sulfides lenses and their stockwork at the Ming deposit are spatially limited to the Rambler Rhyolite dome (Pilote et al. 2017), which was synchronous with Cambro-Ordovician extension within the Baie Verte oceanic tract (Bédard et al. 1998). The three stages of formation of the Ming deposit are shown in Fig. 14 with the elemental change during the evolution of the Ming VMS hydrothermal system. Throughout the evolution of the Ming hydrothermal system, fluids are interpreted to have been controlled by the same synvolcanic faults that developed before and during the deposition of units 1.2 and 1.3 (Pilote et al. 2017). The synvolcanic faults controlled the lateral extent of the alteration into the coherent facies (unit 1.1) and fluid discharge near and at the seafloor. Early temperature increases during fluid evolution

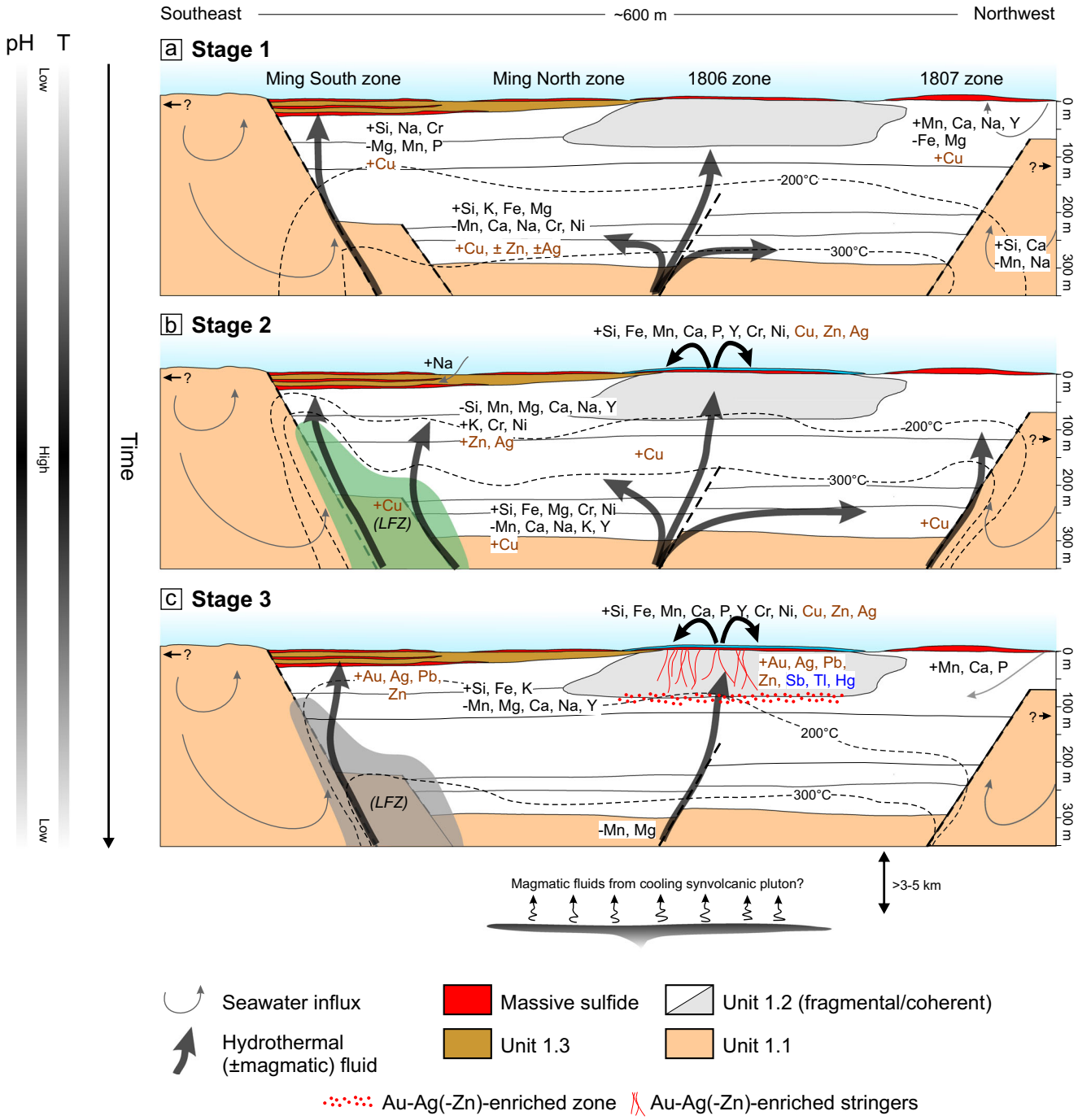

Fig. 14 Schematic reconstruction of the hydrothermal system and its evolution and related elemental changes associated with the formation of the Ming deposit. Gray units represent coherent volcanic lithofacies, whereas the white units represent volcaniclastic lithofacies. **a** Stage 1: early development of low-temperature alteration assemblages (i.e., quartz–calcite ± spessartine, quartz–sericite–chlorite, quartz sericite, and silica-rich layer). **b** Stage 2: waxing and high-temperature alteration assemblages (i.e., quartz–chlorite, quartz–chlorite–sulfide, quartz–chlorite–sericite) associated with introduction of base metals. **c** Stage 3: waning and low-temperature assemblages (i.e., Mn-rich carbonate assemblage, quartz–sericite–sulfide) associated with the introduction of base and precious metals. Isocontours represent interpreted ambient temperatures

resulted in feldspar destruction (hydrolysis) in the felsic host successions, which led to the formation of the quartz–sericite–chlorite and quartz–sericite assemblages, in the southeastern portion of the deposit, below Ming South and 1806 zones. In contrast, the influx of cold seawater containing Ca and Na promoted enrichment in the uppermost part of units 1.2 and 1.3 on the distal edges of the deposit (Fig. 14a). Leached silica due to the slightly acidic alteration that formed the quartz–sericite assemblage precipitated on the paleoseafloor to form the silica-rich layer present above the 1806 zone).

Continuation of hydrothermal activity, combined with an increase in temperature (> 300 °C), produced the chloritic assemblages near the coherent volcanic–volcaniclastic interface due to the fixation and exchange of Mg and Fe from the fluid with pre-existing micas/sericite (Fig. 14b). High-temperature fluids also enabled the transportation of significant Cu, which precipitated within the chloritic assemblages at the contact with the permeable and cooler volcaniclastic rocks of unit 1.2. The overall waning of the temperature is recorded by the overprinting quartz–sericite–sulfide, which also shows the highest enrichment in precious metals and volatiles (Sb, Tl, Hg). The enrichment of this late epithermal-like (Hannington et al. 1999; Huston 2000; Brueckner et al. 2016) overprint was likely controlled by the retention efficiency of the coherent facies found in the 1806 zone (Fig. 14c).

The primary heat source for driving hydrothermal circulation at the Ming deposit remains uncertain. Although it is common for VMS deposits to be spatially and potentially genetically related to a subvolcanic intrusion (Galley 2003), such an intrusion has yet to be found in the vicinity of the Ming deposit. Because hydrothermal alteration and mineralization is restricted to the Rambler Rhyolite formation (Fig. 2), it could be argued that cooling of the felsic dome drove hydrothermal circulation; however, given the limited areal extent of this dome and thickness (< 200 m where it hosts Rambler and East deposits), it is unlikely that it had the heat energy to drive the hydrothermal system that formed the Ming deposit (Cathles 1981). Also, the absence of cross-cutting mafic dykes of the Mount Misery Formation in the Rambler Rhyolite formation makes this an unlikely heat source. Therefore, another deeper, structurally restricted type of heat source has to be considered. At Kidd Creek, for example, given the absence of visible subvolcanic intrusions large enough to contribute to the formation of the ~ 180 Mt deposit (Hannington et al. 2017), workers have proposed structurally controlled upflow driven by the cooling of a ponded ultramafic magma at ~ 15 km depth, much deeper than most VMS-associated subvolcanic intrusions (Galley 1993, 2003). In the Baie Verte Peninsula, VMS-style mineralization occurs at different stratigraphic positions, mainly in the upper and lower portions of the Betts Head and Mount Misery formations, respectively (Betts Cove, Tilt Cove, Big Rambler Pond). These deposits and formations were interpreted to have formed as a result of magmatism associated with forearc extension, resulting in thinning of forearc crust to less than 5 km in places (e.g., Betts Cove Complex; Bédard et al. 1996). This extension would have provided a mechanism to pond magmas at the base of the crust and raise the ambient geothermal gradient. Moreover, forearc extension would have resulted in the formation of extensional faults that could have controlled fluid flow. These two critical ingredients illustrate that the regional tectonics and magmatism were likely critical for driving the hydrothermal circulation that formed the Ming deposit, common in many VMS districts globally (e.g., Piercey 2011).

Comparisons to other deposits in the Rambler Rhyolite formation

Although studies on VMS deposits in the vicinity are scarce to inexistent, Weick (1993) reported mineral assemblages and textures in and outside the sulfide ore of the historical Rambler deposit (Fig. 2) that are very similar to Ming, which some have been validated in the field. The Rambler deposit consists of a northeast plunging ≤ 15-m-thick massive sulfide lens that is hosted by a quartz phenoclastic felsic tuff and coherent rhyodacite. Immediately above the massive sulfide is a dark gray ≤ 1-m-thick magnetic shale layer, which is in turn overlain by mafic flows, a geological setting that is similar to Ming. The Rambler footwall hydrothermal alteration is dominated by a quartz–chlorite–sericite assemblage with localized elongated patches of green micas, inferred as Cr-rich micas by Weick (1993). A strong, systematic depletion in Na and Ca and an enrichment in K is observed in the footwall towards the outcropping massive sulfide (Weick 1993; J-L Pilote, unpubl. data), attributed to the breakdown of feldspars and development of sericite, respectively. The metamorphosed and deformed Rambler massive sulfide (≥ 80 vol% sulfides) consists predominantly of a pyrite–chalcopyrite–sphalerite ± galena assemblage, in which gold is found as inclusions in pyrite or interstitial to recrystallized pyrite grains. Moreover, gold is commonly spatially associated with tellurides and arsenopyrite, some in decomposition textures that resemble what Brueckner et al. (2016) have identified as "symplectite" at Ming. Weick (1993) also pointed out strong color variations in sphalerite, likely owing to differences in Fe content. The latter has been recorded at Ming and was attributed to a change in fluid fS_2 and temperature over the evolution of the VMS formation (Brueckner et al. 2016). Whereas more work is needed at Rambler (and regionally), the broad geological, alteration, mineralogical, and geochemical similarities with Ming, together with its proximity, suffice to suggest that common fluid conditions existed during their formation and that the Rambler Rhyolite formation was fertile to significant Cu(–Au) mineralization (Pilote and Piercey 2018).

Conclusions

Major outcomes from alteration studies are the following:

1. The recognition of nine distinct alteration assemblages and an associated exhalite generation that formed in three paragenetic stages, including the following: (1) low

temperature weak alteration, quartz–calcite ± spessartine, quartz–sericite–chlorite, and quartz–sericite assemblages (stage 1); (2) high-temperature quartz–chlorite, quartz–chlorite–sulfide, and quartz–chlorite–sericite assemblages (stage 2); and (3) low temperature Mn-Ca-rich and quartz–sericite–sulfide assemblages (stage 3). A stratiform silica-rich layer overlaps the 1806 zone and is related to the Ming hydrothermal system.

2. The Mn- and Ca-rich assemblages that underlie the 1807 zone are manifestations of low-temperature mixing of hydrothermal fluids and seawater influx in the footwall rocks, and alteration becomes progressively less intense towards the northwest. These are indications that the 1807 zone represents the northwest fringe of the hydrothermal system.
3. The distribution of the hydrothermal alteration zones is for the most part restricted to the rifted basin developed in the rhyodacitic dome. Fluids discharged were largely controlled by the permeability of the fragmental unit 1.2, where most of the mass changes occurred. The development of the Cu-rich stockwork zone was largely controlled by this coherent–volcaniclastic interface, which formed at depth away from the main discharge zone. Moreover, the lateral distribution of alteration is strongly controlled by synvolcanic faults recognized by the combination of abrupt lithofacies changes and preferentially oriented alteration facies and mineralized zones.
4. The late quartz–sericite–sulfide assemblage is host to Au–Ag-rich veins, suggesting precious metal introduction in the waning stages of the hydrothermal system.
5. The controlling effects on the precious metal-rich fluids appear to include the coherent volcanic rocks. The physical limitations (or perhaps buffering effects) on the fluids may have induced more focused, hence less diffused, metal transport in low temperature conditions. We speculate that the combination of higher water/rock ratio at the base of these coherent facies and the impermeable barrier of the latter may also have played a critical role in providing near neutral (higher pH) conditions and a trap to the ascending fluids.
6. The driving mechanism to the hydrothermal circulation was likely the combination of a deep (≥ 5 km) heat source and from the cooling of the ascending and emplacement of the rhyodacitic Rambler Rhyolite dome. We speculate that the thin nature of the Baie Verte oceanic tract during its formation, hence the high geothermal gradient, could have compensated for the possible absence of subvolcanic intrusions in the area.

Acknowledgments The authors would like to thank Rambler Metals and Mining Ltd. and geologists Larry Pilgrim and Paul Legrow for providing access to the underground workings, drill core, data, and samples and Pam King, Lakmali Hewa, and Wanda Aylward of CREAIT at Memorial University of Newfoundland (MUN) for their technical support and guidance during the multiple stages of sample preparation and geochemical and EPMA analyses. We appreciate the technical support from and insightful discussions with J. Cloutier (CODES/University of Tasmania) and S.M. Brueckner (Laurentian University). This manuscript was significantly improved through the reviews of A. Galley, K. Kelley, and an anonymous reviewer and the constructive comments of the editor-in chief, G. Beaudoin.

Funding information This research was funded by grants to S.J. Piercey, including an NSERC Discovery Grant, and the NSERC-Altius Industrial Research Chair in Mineral Deposits funded by NSERC, Altius Minerals Inc., and the Research and Development Corporation of Newfoundland and Labrador. This study was also funded in part by the Geological Survey of Canada's Targeted Geoscience Initiative Program.

References

Arnórsson S, Stefánsson A, Bjarnarson JÖ (2007) Fluid-fluid interactions in geothermal systems. In: Liebscher A, Heinrich CA (ed) Fluid–fluid interactions, Reviews in Mineralogy and Geochemistry 65, pp 259–312

Bailey J (2002) Chemostratigraphy surrounding the Ming VMS mineralization in the Northern Pacquet Harbour Group (PHG) and correlations with the southern PHG, Baie Verte Peninsula, Newfoundland. Dissertation, Memorial University of Newfoundland

Barrett TJ, MacLean WH (1994) Chemostratigraphy and hydrothermal alteration in exploration for VHMS deposits in greenstones and younger volcanic rocks. Short Course Notes, Geological Association of Canada 11:433–467

Bédard JH, Escayola M (2010) The advocate ophiolite mantle, Baie Verte, Newfoundland; regional correlations and evidence for metasomatism. Can J Earth Sci 47:237–253. https://doi.org/10.1139/e10-004

Bédard JH, Lauzière K, Sangster A, Boisvert E, Tellier M, Tremblay A, Dec T (1996) Geological map of the Betts Cove ophiolitic massif and its cover rocks. Geological Survey of Canada, Canadian Geoscience Map 3271, scale 1:20 000

Bédard JH, Lauzière K, Tremblay A, Sangster A (1998) Evidence for forearc seafloor-spreading from the Betts Cove ophiolite, Newfoundland: oceanic crust of boninitic affinity. Tectonophysics 284:233–245. https://doi.org/10.1016/s0040-1951(97)00182-0

Brueckner SM, Piercey SJ, Sylvester PJ, Pilgrim L, Maloney S, Hyde D, Ogilvie G (2011) Stratigraphy, mineralogy, geochemistry, and genesis of an Au-rich volcanogenic massive sulfide (VMS) system from the Baie Verte Peninsula, NW Newfoundland, Canada: The 1806 zone as an example from the Ming Mine, Rambler Camp. In: Deschênes G, Dimitrakopoulos R, Bouchard J (eds) World Gold 2011, Canadian Institute of Mining, Metallurgy and Petroleum, Montreal, QC, Canada, pp 899–911

Brueckner SM, Piercey SJ, Sylvester PJ, Maloney S, Pilgrim L (2014) Evidence for syngenetic precious metal enrichment in an Appalachian volcanogenic massive sulfide system: the 1806 zone, Ming mine, Newfoundland, Canada. Econ Geol 109:1611–1642. https://doi.org/10.2113/econgeo.109.6.1611

Brueckner SM, Piercey SJ, Layne GD, Piercey G, Sylvester PJ (2015) Variations of sulphur isotope signatures in sulphides from the metamorphosed Ming Cu(-Au) volcanogenic massive sulphide deposit, Newfoundland Appalachians, Canada. Mineral Deposita 50:619–640. https://doi.org/10.1007/s00126-014-0567-7

Brueckner SM, Piercey SJ, Pilote J-L, Layne GD, Sylvester PJ (2016) Mineralogy and mineral chemistry of the metamorphosed and precious metal-bearing Ming deposit, Canada. Ore Geol Rev 72:914–939. https://doi.org/10.1016/j.oregeorev.2015.09.016

Buschette MJ, Piercey SJ (2016) Hydrothermal alteration and lithogeochemistry of the boundary volcanogenic massive sulphide deposit, central Newfoundland, Canada. Can J Earth Sci 53:506–527. https://doi.org/10.1139/cjes-2015-0237

Castonguay S, Skulski T, van Staal CR, Currie M (2009) New insights on the structural geology of the Pacquet Harbour group and Point Rousse complex, Baie Verte peninsula, Newfoundland. Newfoundland and Labrador Department of Natural Resources, Geological Survey Report 09-1:147–158

Castonguay S, van Staal CR, Joyce N, Skulski T, Hibbard JP (2014) Taconic metamorphism preserved in the Baie Verte Peninsula, Newfoundland Appalachians: geochronological evidence for ophiolite obduction and subduction and exhumation of the leading edge of the Laurentian (Humber) margin during closure of the Taconic seaway. Geosci Can 14:459–482. https://doi.org/10.12789/geocanj.2014.41.055

Cathles LM (1981) Fluid flow and genesis of hydrothermal ore deposits. In: Skinner BJ (ed) Economic Geology Seventy-Fifth Anniversary Volume: 424–457. https://doi.org/10.5382/av75.13

Cawood PA, van Gool JAM, Dunning GR (1996) Geological development of eastern Humber and western Dunnage zones; Corner Brook-Glover Island region, Newfoundland. Can J Earth Sci 33:182–198

Date J, Watanabe Y, Saeki Y (1983) Zonal alteration around the Fukazawa Kuroko deposits, Akita Prefecture, northern Japan. Economic Geology Monograph 5:365–386

Deer WA, Howie RA, Zussman J (2013) An introduction to the rock forming minerals. Longman, London, p 528

DeWolfe YM (2009) Physical volcanology, petrology and tectonic setting of intermediate and mafic volcanic and intrusive rocks in the Flin Flon volcanogenic massive sulphide (VMS) district, Manitoba, Canada. Dissertation, Laurentian University

Doyle MG, Allen RL (2003) Subsea-floor replacement in volcanic-hosted massive sulfide deposits. Ore Geol Rev 23:183–222. https://doi.org/10.1016/s0169-1368(03)00035-0

Dubé B, Mercier-Langevin P, Hannington MD, Lafrance B, Gosselin G, Gosselin P (2007) The LaRonde Penna world-class Au-rich volcanogenic massive sulfide deposit, Abitibi, Quebec; mineralogy and geochemistry of alteration and implications for genesis and exploration. Econ Geol 102:633–666. https://doi.org/10.2113/gsecongeo.102.4.633

Dunning GR, Krogh TE (1985) Geochronology of ophiolites of the Newfoundland Appalachians. Can J Earth Sci 22:1659–1670. https://doi.org/10.1139/e85-174

Gale GH (1971) An investigation of some sulfide deposits of the Rambler Area, Newfoundland. Dissertation, University of Durham

Galley AG (1993) Characteristics of semi-conformable alteration zones associated with volcanogenic massive sulphide districts. J Geochem Explor 48:175–200. https://doi.org/10.1016/0375-6742(93)90004-6

Galley AG (2003) Composite synvolcanic intrusions associated with Precambrian VMS-related hydrothermal systems. Mineral Deposita 38:443–473. https://doi.org/10.1007/s00126-002-0300-9

Gemmell JB, Large RR (1992) Stringer system and alteration zones underlying the Hellyer volcanogenic massive sulfide deposit, Tasmania, Australia. Econ Geol 87:620–649. https://doi.org/10.2113/gsecongeo.87.3.620

Gibson H, Morton RL, Hudak GJ (1999) Submarine volcanic processes, deposits, and environments favorable for the loaction of volcanic-associated massive sulfide deposits. In: Barrie CT, Hannington MD (ed) Volcanic-associated massive sulfide deposits: processes and examples in modern and ancient settings, Reviews in Economic Geology 8, pp 13–51

Grant JA (1986) The Isocon diagram: a simple solution to Gresens' equation for metasomatic alteration. Econ Geol 81:1976–1982

Hajash A, Chandler GW (1982) An experimental investigation of high-temperature interactions between seawater and rhyolite, andesite, basalt and peridotite. Contrib Mineral Petrol 78:240–254. https://doi.org/10.1007/bf00398919

Hannington MD, Poulsen KH, Thompson JFH, Sillitoe RH (1999) Volcanogenic gold in the massive sulfide environment. In: Barrie CT, Hannington MD (eds) Volcanic-associated massive sulfide deposits: processes and examples in modern and ancient settings, Reviews in Economic Geology, vol 8, pp 325–351

Hannington MD, Kjarsgaard IM, Galley AG, Taylor B (2003a) Mineral-chemical studies of metamorphosed hydrothermal alteration in the Kristineberg volcanogenic massive sulfide district, Sweden. Mineral Deposita 38:423–442. https://doi.org/10.1007/s00126-002-0299-y

Hannington MD, Santaguida F, Kjarsgaard IM, Cathles LM (2003b) Regional-scale hydrothermal alteration in the Central Blake River Group, western Abitibi subprovince, Canada: implications for VMS prospectivity. Mineral Deposita 38:393–422. https://doi.org/10.1007/s00126-002-0298-z

Hannington MD, de Ronde CEJ, Petersen S (2005) Sea-floor tectonics and submarine hydrothermal systems. In: Hedenquist JW, Thompson, J.F.H., Goldfarb, R.J., Richards, J.P. (ed) Economic Geology 100th Anniversary Volume, pp 111–141

Hannington MD, Gemmell T, Monecke T (2017) The Kidd Creek volcanogenic massive sulfide deposit – an update. Rev Econ Geol 19:81–102

Hart TR, Gibson HL, Lesher CM (2004) Trace element geochemistry and petrogenesis of felsic volcanic rocks associated with volcanogenic massive Cu-Zn-Pb sulfide deposits. Econ Geol 99:1003–1013. https://doi.org/10.2113/gsecongeo.99.5.1003

Herrmann W, Hill AP (2001) The origin of chlorite-tremolite-carbonate rocks associated with the Thalanga volcanic-hosted massive sulfide deposit, North Queensland, Australia. Econ Geol 96:1149–1173

Herrmann W, Blake MD, Doyle MG, Huston DL, Kamprad J, Merry N, Pontual S (2001) Short wavelength infrared (SWIR) spectral analysis of hydrothermal alteration zones associated with base metal sulfide deposits at Rosebery and Western Tharsis, Tasmania, and Highway-Reward, Queensland. Econ Geol 96:939–955

Hey MH (1954) A new review of the chlorites. Mineral Mag 30:277–292

Hibbard J (1983) Geology of the Baie Verte Peninsula, Newfoundland, vol 2. Newfoundland Department of Mines and Energy, Geological Survey, Memoir 279 p

Huston DL (1993) The effect of alteration and metamorphism on wall rocks to the Balcooma and Dry River South volcanic-hosted massive sulfide deposits, Queensland, Australia. J Geochem Explor 48:277–307. https://doi.org/10.1016/0375-6742(93)90008-a

Huston DL (2000) Gold in volcanic-hosted massive sulfide deposits: distribution, genesis, and exploration. In: Hagemann SG, Brown, P.E. (ed) Gold in 2000, Reviews in Economic Geology 13, pp 401–426

Ishikawa Y, Sawaguchi T, Iwaya S, Horiuchi M (1976) Delineation of prospecting targets for Kuroko deposits based on modes of volcanism of underlying dacite and alteration halos. Min Geol 26:105–117

Krauskopf KB, Bird DK (1995) Introduction to geochemistry. McGraw-Hill, New York

Large RR (1992) Australian volcanic-hosted massive sulfide deposits: features, styles, and genetic models. Econ Geol 87:471–510

Large RR, Allen RL, Blake MD, Herrmann W (2001a) Hydrothermal alteration and volatile element halos for the Rosebery K Lens volcanic-hosted massive sulfide deposit, western Tasmania. Econ Geol 96:1055–1072. https://doi.org/10.2113/gsecongeo.96.5.1055

Large RR, Gemmell JB, Paulick H, Huston DL (2001b) The alteration box plot: a simple approach to understanding the relationship between alteration mineralogy and lithogeochemistry associated with volcanic-hosted massive sulfide deposits. Econ Geol 96:957–971. https://doi.org/10.2113/gsecongeo.96.5.957

Large RR, McPhie J, Gemmell JB, Herrmann W, Davidson GJ (2001c) The spectrum of ore deposit types, volcanic environments, alteration halos, and related exploration vectors in submarine volcanic successions: some examples from Australia. Econ Geol 96:913–938

Lesher CM, Goodwin AM, Campbell IH, Gorton MP (1986) Trace-element geochemistry of ore-associated and barren, felsic metavolcanic rocks in the Superior Province, Canada. Can J Earth Sci 23:222–237

Lydon JW (1988) Volcanogenic massive sulphide deposits part 2: genetic models. Geosci Can 15:43–65

Lydon JW (1996) Characteristics of volcanogenic massive sulphide deposits; interpretations in terms of hydrothermal convection systems and magmatic hydrothermal systems. Boletin Geologico y Minero 107:215–264

Mercier-Langevin P, Dubé B, Hannington MD, Davis DW, Lafrance B, Gosselin G (2007) The LaRonde Penna Au-rich volcanogenic massive sulfide deposit, Abitibi greenstone belt, Quebec: part I. Geology and geochronology. Econ Geol 102:585–609

Mercier-Langevin P, Lafrance B, Bécu V, Dubé B, Kjarsgaard I, Guha J (2014) The Lemoine auriferous volcanogenic massive sulfide deposit, Chibougamau Camp, Abitibi Greenstone Belt, Quebec, Canada: geology and genesis. Econ Geol 109:231–269. https://doi.org/10.2113/econgeo.109.1.231

Monecke T, Petersen S, Hannington MD (2014) Constraints on water depth of massive sulfide formation: evidence from modern seafloor hydrothermal systems in arc-related settings. Econ Geol 109:2079–2101. https://doi.org/10.2113/econgeo.109.8.2079

Nakamura N (1974) Determination of REE, Ba, Fe, Mg, Na and K in carbonaceous and ordinary chondrites. Geochim Cosmochim Acta 38:757–775. https://doi.org/10.1016/0016-7037(74)90149-5

Pearce JA (1996) A user's guide to basalt discrimination diagrams. Short Course Notes, Geological Association of Canada 12:79–113

Pearce JA, Baker PE, Harvey PK, Luff IW (1995) Geochemical evidence for subduction fluxes, mantle melting and fractional crystallization beneath the South Sandwich island arc. J Petrol 36:1073–1109

Piercey SJ (2011) The setting, style, and role of magmatism in the formation of volcanogenic massive sulfide deposits. Mineral Deposita 46:449–471. https://doi.org/10.1007/s00126-011-0341-z

Piercey SJ, Peter JM, Herrington R (2015) Zn-rich volcanogenic massive sulfide (VMS) deposits. In: Archibald SM, Piercey SJ (ed). Current perspectives on zinc deposits. Irish Association for Economic Geology Special Publication on Zinc Deposits, pp 37–57

Pilgrim L (2009) Mineral resource estimate for the Ming Mine, Newfoundland, Canada. Rambler Metals and Mining Canada Ltd., Technical Report NI43–101, 114 p

Pilote J-L, Piercey SJ (2018) Petrogenesis of the rambler rhyolite formation: controls on the Ming VMS deposit and geodynamic implications for the Taconic seaway, Newfoundland Appalachians, Canada. Am J Sci 318:640–683

Pilote J-L, Piercey SJ, Mercier-Langevin P (2014) Stratigraphy and hydrothermal alteration of the Ming Cu-Au volcanogenic massive-sulphide deposit, Baie Verte peninsula, Newfoundland. Geological Survey of Canada, Current Research, Report 2014–2017, 18 p. https://doi.org/10.4095/295145

Pilote J-L, Piercey SJ, Brueckner SM, Grant D (2016) Resolving the relative timing of Au enrichment in volcanogenic massive sulfide deposits using scanning electron microscopy-mineral liberation analyzer: empirical evidence from the Ming deposit, Newfoundland, Canada. Econ Geol 111:1495–1508. https://doi.org/10.2113/econgeo.111.6.1495

Pilote J-L, Piercey SJ, Mercier-Langevin P (2017) Volcanic and structural reconstruction of the deformed and metamorphosed Ming volcanogenic massive sulfide deposit, Canada: implications for ore zone geometry and metal distribution. Econ Geol 112:1305–1332. https://doi.org/10.5382/econgeo.2017.4511

Reed MH (1997) Hydrothermal alteration and its relationship to ore fluid composition. In: Barnes HL (ed) Geochemistry of hydrothermal ore deposits, 3rd edn. John Wiley & Sons, New York, pp 303–365

Rieder M, Cavazzini G, D'yakonov YS, Frank-Kemenetskii VA, Gottardi G, Guggenheim S, Koval PV, Müller G, Neiva AMR, Radoslovich EW, Robert JL, Sassi FP, Takeda H, Weiss Z, Wones DR (1999) Nomenclature of the micas. Mineralogical Magazine 63:267–279

Ross P-S, Bédard JH (2009) Magmatic affinity of modern and ancient subalkaline volcanic rocks determined from trace-element discriminant diagrams. Can J Earth Sci 46:823–839. https://doi.org/10.1139/e09-054

Schardt C, Cooke DR, Gemmell JB, Large RR (2001) Geochemical modeling of the zoned footwall alteration pipe, Hellyer volcanic-hosted massive sulfide deposit, Western Tasmania, Australia. Econ Geol 96:1037–1054. https://doi.org/10.2113/gsecongeo.96.5.1037

Skulski T et al (2010) Tectonostratigraphy of the Baie Verte oceanic tract and its ophiolite cover sequence on the Baie Verte Peninsula. Newfoundland and Labrador Department of Natural Resources, Geological Survey Report 10-1:315–335

Skulski T, Castonguay S, Kidd WSF, McNicoll VJ, van Staal CR, Hibbard JP (2015) Geology, Baie Verte and parts of Fleur de Lys, Newfoundland and Labrador, NTS 12-H/16 and part of NTS 12-I/1; Geological Survey of Canada, Canadian Geoscience Map 159, scale 1:50 000. https://doi.org/10.4095/295865

Spitz G, Darling R (1978) Major and minor element lithogeochemical anomalies surrounding the Louvem copper deposit, Val d'Or, Quebec. Can J Earth Sci 15:1161–1169. https://doi.org/10.1139/e78-122

Sun SS, McDonough WF (1989) Chemical and isotopic systematics of oceanic basalts; implications for mantle composition and processes. Geol Soc Spec Publ 42:313–345

Sverjensky DA (1984) Europium redox equilibria in aqueous solution. Earth Planet Sci Lett 67:70–78. https://doi.org/10.1016/0012-821X(84)90039-6

Thompson AJB, Hauff PL, Robitaille JA (1999) Alteration mapping in exploration; application of short-wave infrared (SWIR) spectroscopy. SEG Newsletter 39:1–27

Tuach J, Kennedy MJ (1978) The geologic setting of the Ming and other sulfide deposits, Consolidated Rambler Mines, Northeast Newfoundland. Econ Geol 73:192–206. https://doi.org/10.2113/gsecongeo.73.2.192

van Staal CR, Barr SM (2012) Lithosperic architecture and tectonic evolution of the Canadian Appalachians and associated Atlantic margin. In: Percival JA, Cook FA, Clowes RM (eds) Tectonic styles in Canada: the LITHOPROBE perspective. Geological Association of Canada, Special Paper 49, pp 41–95

van Staal CR, Chew DM, Zagorevski A, McNicoll V, Hibbard J, Skulski T, Escayola MP, Castonguay S, Sylvester PJ (2013) Evidence of Late Ediacaran hyperextension of the Laurentian Iapetan margin in the Birchy Complex, Baie Verte Peninsula, northwest Newfoundland: implications for the opening of Iapetus, formation of peri-Laurentian microcontinents and Taconic-Grampian orogenesis. Geosci Can 40:94–117

Waldron JWF, van Staal CR (2001) Taconian Orogeny and the accretion of the Dashwoods Block; a peri-Laurentian microcontinent in the Iapetus Ocean. Geology 29:811–814

Walshe JL, Solomon M (1981) An investigation into the environment of formation of the volcanic-hosted Mt. Lyell copper deposits using geology, mineralogy, stable isotopes, and a six-component chlorite solid-solution model. Econ Geol 76:246–284

Weick RJ (1993) Petrography and stable isotope geochemistry of alteration and mineralization in the Rambler volcanogenic massive sulphide deposit, Baie Verte, Newfoundland. Dissertation, Memorial University of Newfoundland

Winchester JA, Floyd PA (1977) Geochemical discrimination of different magma series and their differentiation products using immobile elements. Chem Geol 20:325–343